

University of Alberta

**High-Resolution Imaging of the Mantle Transition Zone beneath Japan
from Sparse Receiver Functions**

by

Christian Escalante

A thesis submitted to the Faculty of Graduate Studies and Research
in partial fulfillment of the requirements for the degree of

Master of Science

in

Geophysics

Department of Physics

©Christian Escalante

Fall 2012

Edmonton, Alberta

Permission is hereby granted to the University of Alberta Libraries to reproduce single copies of this thesis and to lend or sell such copies for private, scholarly or scientific research purposes only. Where the thesis is converted to, or otherwise made available in digital form, the University of Alberta will advise potential users of the thesis of these terms.

The author reserves all other publication and other rights in association with the copyright in the thesis and, except as herein before provided, neither the thesis nor any substantial portion thereof may be printed or otherwise reproduced in any material form whatsoever without the author's prior written permission.

To my lovely wife and children

ABSTRACT

A new approach to estimate high-resolution receiver functions using a simultaneous iterative time-domain sparse deconvolution is presented. To test its functionality and reliability, several experiments were conducted with synthetic and real seismological data. Furthermore, this technique was employed to obtain a high-resolution image of the mantle transition zone discontinuities beneath Japan. The results show a locally elevated 410-km discontinuity with a topographic relief of up to 10 km; conversely, the 660-km discontinuity shows a large depression of up to ~30 km in regions coincident with the subducting Pacific plate. These results are consistent with previous receiver function and tomographic studies showing a flat lying slab in this region. It is still debatable whether parts of the deflected slab is sinking into the lower mantle or not; since this is not clearly observed from the results. But it appears that the 660-km discontinuity deflection extends further to the west into the Korean Peninsula.

ACKNOWLEDGEMENTS

It is difficult to overstate my gratitude to my supervisor, Dr. Moritz Heimpel. For his patience, enthusiasm, sound advice, and encouragement. Without his support and assistance, it would have not been possible to complete this thesis.

I would like to thank Dr. Mauricio Sacchi, Dr. Jeff Gu, Dr. Claire Currie, and Dr. Takashi Tonegawa (Earthquake Research Institute, University of Tokyo, Japan) for their kind assistance, wise advice, and fruitful discussions. Also, I want to thank the Japanese National Research Institute for Earth Science and Disaster Prevention (NIED) for providing the F-NET data.

I am also indebted to my many colleagues for their endless help and providing a stimulating and fun environment. I am especially grateful to Somanath Misra, Ahmet Okeler, Keith Brzak, Natalia Gomez, and Wolfgang Engler. Thank you for their friendship and always enriching discussions and contributions.

Finally, and most importantly, I wish to thank my wife (Doris) and children (Emily & Nicholas) for all their love, understanding and support. They have been, always, my pillar, my joy and my guiding light.

TABLE OF CONTENTS

CHAPTER 1: INTRODUCTION	1
1.1 Introduction.....	1
1.2 References.....	6
CHAPTER 2: JAPAN SUBDUCTION ZONE AND TECTONIC SETTING	11
2.1 Introduction.....	11
2.2 Tectonic Setting	12
2.3 Japanese Subduction Zone.....	18
2.4 References.....	23
CHAPTER 3: SIMULTANEOUS ITERATIVE TIME-DOMAIN SPARSE DECONVOLUTION TO TELESEISMIC RECEIVER FUNCTIONS	27
3.1 Introduction.....	27
3.2 Sparse Deconvolution	29
3.3 Synthetic Experiments	36
3.4 Estimation of receiver functions in Southern Japan.....	41
3.5 Conclusion	49
3.6 References.....	49
CHAPTER 4: HIGH-RESOLUTION IMAGING OF THE MANTLE TRANSITION ZONE BENEATH JAPAN FROM SPARSE RECEIVER FUNCTIONS	54
4.1 Introduction.....	54
4.2 Seismological data, Data Selection, and RF Processing.....	57
4.2.1 F-NET Broadband Seismograph Network.....	57

4.2.2	Data Selection	59
4.2.3	P-Wave Travel Time Picking.....	63
4.2.4	Receiver Function Processing.....	64
4.3	Results.....	66
4.4	Discussions	71
4.5	Conclusions.....	73
4.6	References.....	75
CHAPTER 5: CONCLUSIONS		79
5.1	Conclusions.....	79
5.2	Future Work.....	80
5.3	References.....	81
APPENDIX A: F-NET BROADBAND SEISMOGRAPH NETWORK.....		83

LIST OF FIGURES

- Figure 1.1:** Small phase proportions (blue left axis) in a typical mantle bulk composition. Phases are: plagioclase (plg), spinel (sp), olivine (ol), orthopyroxene (opx), clinopyroxene (cpx), high-pressure Mg-rich clinopyroxene (hpcpx), garnet (gt), wadsleyite (wa), ringwoodite (ri), akimotoite (ak), Calcium silicate perovskite (capv), Magnesium silicate perovskite (pv), and ferropericlasite (fp). From Stixrude & Lithgow-Bertelloni 2005a, 2005b..... 3
- Figure 1.2:** Calculated density and elastic wave velocities for different geotherms for pyrolite-like compositions with (a) 3% Al₂O₃ and (b) 5% Al₂O₃. Calculations are compared with the PREM seismological model (Dziewonski & Anderson 1981). Reproduced from Weidner & Wang 1998. 4
- Figure 1.3:** Cartoon showing the possible behaviour of seismic discontinuities in the transition when interacting with a subducting slab. Modified from Christensen (1995)..... 5
- Figure 2.1:** Plate tectonics of the Japanese arc system. (a) Plate tectonic framework of Northeastern Asia (modified after Wei & Seno 1998). (b) Main part of the Japanese arc system, showing the distribution of the four big islands. (c) Plate boundaries of the Japanese arc system. Note that central Honshu shows complex microplate tectonics dominated by the median tectonic line (MTL), right-lateral motion, and bookshelf-type rotation tectonics (from Taira 2001)..... 15
- Figure 2.2:** GPS vector data (1997 - 1999) from GEONET, the GPS network maintained by the Geography Survey Institute of Japan, showing crustal deformation of the Japanese arc system (after Sagiya *et al.* 2000). Modified from Taira 2001. 16
- Figure 2.3:** Paleogeographic reconstruction since 103 Ma (after Taira *et al.* 1989). Reproduced from Taira 2001..... 17
- Figure 2.4:** Vertical cross-section of (a) *P*-wave velocity, (b) *S*-wave velocity, and (c) Poisson's ratio perturbations along a profile as shown in the inset map (Zhao *et al.* 2009, 2011). Red denotes low velocity and high Poisson's ratio, while blue denotes high velocity and low Poisson's ratio. Red triangles denote active arc volcanoes. The reverse triangles show the

location of the Japan Trench. Small white dots shown earthquakes which occurred within a 15-km width along the profile. The curved lines show the Conrad and Moho discontinuities and the upper boundary of the subducting Pacific slab. The dashed lines denote the estimated low boundary of the Pacific slab..... 19

Figure 3.1: Probability distributions for Gaussian, exponential, and Cauchy functions that have a mean value of 0, and a variance value of 4. 31

Figure 3.2: Estimated receiver functions for a simple two-layer velocity model: (1) velocity model (solid and dashed lines indicate P and S velocities, respectively); (b) vertical-component seismogram; (c) radial-component seismogram; (d) receiver function obtained after applying water-level deconvolution (Ammon 1991); (e) computed receiver function after applying the least-squares deconvolution (Gurrola *et al.* 1995) and (f) estimated receiver function using the sparse deconvolution (this study). P_s conversions and multiples are indicated. 38

Figure 3.3: Simplified diagram showing the ray paths of the main conversions (P_s) and its multiples (P_sP_s , P_pS_s and P_pP_s). Except from the first arrival (P), upper-case letters indicate upgoing travel paths, and lower-case letters indicate downgoing travel paths (modified from Ammon 1991). 39

Figure 3.4: Estimated receiver functions for a multilayer velocity model: (a) velocity model (solid and dashed lines indicate P and S velocities, respectively); (b) vertical-component seismogram; (c) radial-component seismogram; (d) receiver function obtained from water-level deconvolution (Ammon 1991); (e) computed receiver function from least-squares deconvolution (Gurrola *et al.* 1995) and (f) estimated receiver function using the sparse deconvolution (this study)..... 40

Figure 3.5: Same as in Figure 3.2 but in this case we added noise to the vertical and radial component seismograms (signal-to-noise ratio = 0.1)..... 41

Figure 3.6: Azimuthal orthographic projection of teleseismic events recorded at station ABU, Southern Japan, during 2003. Only events from four azimuthal directions were used in this study. Equidistant lines at every 30° are shown by concentric circles. Solid lines represent ray paths..... 42

Figure 3.7: A comparison of the estimated receiver function for the NE azimuthal direction using least-squares deconvolution and the sparse deconvolution approach. (a) Receiver function obtained from least-squares

deconvolution (Gurrola *et al.* 1995). (b) Trade-off curves for the least-squares approach (dashed line) and the sparse deconvolution approach (solid line). The dotted line marks the hyperparameters (intercepts with trade-off curves) used to estimate the receiver functions that produce the same misfit. (c) Receiver function determined using the sparse deconvolution (solid line); the results displayed in (a) is also shown (dashed line) for a better comparison. 44

Figure 3.8: Receiver functions computed for different hyperparameters α and μ . All the resulting models ensure the same misfit. Higher α values enforce sparseness in the model. Conversely, the receiver function approaches the damped least-squares when α approaches to 0. 45

Figure 3.9: Estimated radial-component seismograms from events located in the NE azimuthal direction. (a) Vertical-component seismograms; (b) receiver functions estimated using time-domain sparse deconvolution and (c) estimated (dashed lines) and observed (solid lines) radial-component seismograms. The epicentral distances are also indicated. 46

Figure 3.10: Receiver functions at station ABU (Southern Japan) estimated by the simultaneous iterative sparse deconvolution for all azimuthal directions. The number of events used to compute the receiver functions are also indicated. There are slight differences among the receiver functions, especially in the timing of the phases due to the lack of distance and heterogeneity corrections to the receiver functions. 48

Figure 4.1: F-NET broadband seismograph network. Blue squares indicate F-NET stations. Thick and thin red lines denote the plate boundaries and contour depths of the top surface of the Pacific slab determined by distribution of deep and intermediate-deep earthquakes, respectively. 58

Figure 4.2: Distribution of the teleseismic events used in this work. Distances (in degrees) are with respect to the centre of the study area. Red stars and blue triangles indicate the location of teleseismic events and F-NET seismic stations, respectively. Black lines indicate 5° azimuthal bins used for computing the sparse receiver functions for station ABU, southern Japan. 60

Figure 4.3: Piercing points of Ps converted phases at a depth of 410 km indicated by purple squares. Blue triangles indicate F-NET station locations. Thick and thin red lines indicate plate boundaries and contour depths corresponding to the top surface of the subducting slabs obtained

from the distribution of deep and intermediate-deep earthquakes, respectively.	61
Figure 4.4: Same as Figure 4.3 but at 660 km. Green squares and blue triangles indicate piercing points of <i>Ps</i> converted phases and F-NET station locations.	62
Figure 4.5: Vertical component broadband recordings for an event at the Aleutian Islands. The traces are aligned with respect to their relative arrival times. Note the resulting signal coherence.	64
Figure 4.6: Estimated sparse receiver functions for station ABU, southern Japan. Each receiver function corresponds to an individual azimuthal bin. Identification of <i>Ps</i> converted phases at the 410 and 660-km discontinuity is indicated. Lower panel shows the stacked receiver function.	65
Figure 4.7: Depth distribution of the 410-km discontinuity. Red triangles indicate F-NET station locations. Black dotted lines (contour depths) correspond to the top surface of the subducting slabs obtained from the distribution of deep and intermediate-deep earthquakes.	68
Figure 4.8: Same as Figure 4.6 but for the 660-km discontinuity.	69
Figure 4.9: Thickness of the mantle transition zone. Symbols and lines are the same as in Figure 4.6.	70
Figure 4.10: East-West vertical cross sections of P-wave velocity perturbations along latitudes 43, 39, and 30, where the horizontal slab (i.e. stagnant slab) extends over a distance of 800 to 1000 km above the 660-km discontinuity. From Fukao et al. (2009)	74

CHAPTER 1

INTRODUCTION

1.1 Introduction

The Earth's mantle encloses many of the most intriguing, and still unsolved problems in Earth dynamics. Its convection, a chaotic process in which hot material upwells driven by buoyancy forces (Oxburgh & Turcotte, 1978), while cooler and heavier material sinks back into the mantle, is the driving force of many of the processes that occur in the Earth from plate tectonics to orogenesis.

A prominent feature that lies in the upper mantle is the transition zone, which represents a dynamical region where seismic wave speed and density increase abruptly with depth. Several studies have focused on this zone due to its importance in understanding the nature of the Earth's convective regime. Its upper and lower boundaries, referred to as the 410 and 660-km discontinuities, are considered to be the results of pressure- and temperature-induced phase changes in the olivine system (Figure 1.1). At ~14 GPa (410 km depth), the $(\text{Mg,Fe})_2\text{SiO}_4$ olivine (also referred to as α -phase olivine) transforms into a denser structure Wadsleyite $(\text{Mg, Fe}^{2+})_2\text{SiO}_4$, sometimes referred to as β -phase or modified spinel. At around 17.5 GPa (520 km depth), Wadsleyite transforms into Ringwoodite, sometimes termed γ -phase or silicate spinel. Finally, at approximately 24 GPa (660 km depth) Ringwoodite breaks down to an assemblage of perovskite-structured $(\text{Mg,Fe})\text{SiO}_3$ and $(\text{Mg,Fe})\text{O}$ magnesiowüstite

which marks the end of the transition and the beginning of the lower mantle (Bina & Silver 1990; Frost, 2008).

The transition zone discontinuities play a significant role in characterizing major changes in seismic velocity, rheology, and potentially chemical composition (Ringwood & Irifune 1988; Stixrude 1997; Shearer 2000). However, many intriguing problems are still unsolved or have unclear solutions. For instance, at the 410-km discontinuity, the seismic velocity gradient is too large for a typical pyrolitic mantle (Duffy *et al.* 1995; Li *et al.* 1998; Liu *et al.*, 2005; Zha *et al.* 1997) suggesting that chemical exchanges of non-transforming phases with olivine and wadsleyite may sharpen this discontinuity significantly (Stixrude 1997; 2007). Other factors, such as temperature variations, might also play a role in affecting the character of the 410-km discontinuity. Helffrich & Bena (1991) observed that decreasing temperature with depth, and iron enrichment both increase the width of the discontinuity (Akaogi *et al.* 1989; Fei *et al.* 1991). Recent studies at subduction zones show that the mantle wedge is significantly slower than the subducting slab and several low velocity regions are observed overlaying the 410-km discontinuity suggesting the presence of partial melt associated with water enrichment (Revenaugh & Sipkin 1994; Song *et al.* 2004; Tonegawa *et al.* 2005, 2008). This indicates that subducting slabs can carry water down to these depths.

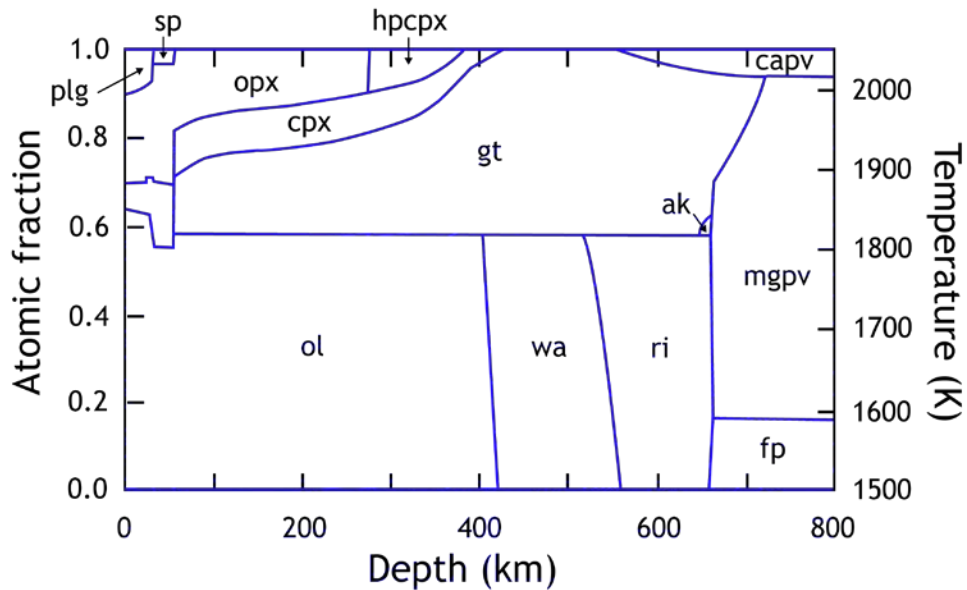


Figure 1.1: Small phase proportions (blue left axis) in a typical mantle bulk composition. Phases are: plagioclase (plg), spinel (sp), olivine (ol), orthopyroxene (opx), clinopyroxene (cpx), high-pressure Mg-rich clinopyroxene (hpcpx), garnet (gt), wadsleyite (wa), ringwoodite (ri), akimotoite (ak), Calcium silicate perovskite (capv), Magnesium silicate perovskite (pv), and ferropericlase (fp). From Stixrude & Lithgow-Bertelloni 2005a, 2005b.

The 660-km discontinuity represents the boundary between the upper and lower mantle and may represent a barrier to whole mantle convection. It is also quite complex in structure (Figure 1.2) and composition. For instance, several seismological observations identify two seismic velocity jumps (instead of one) similar in magnitude. This has been interpreted as a doubled discontinuity with a very short separation between the two ends (Simmons & Gurrola 2000). It may also represent multiple phase transitions, at these depths, consistent with numerical calculations of mantle velocities (Vacher *et al.* 1998) that show that multiple phase changes could result in velocity jumps between ~660 and 720 km; however, the resulting geodynamical implications are still not well understood.

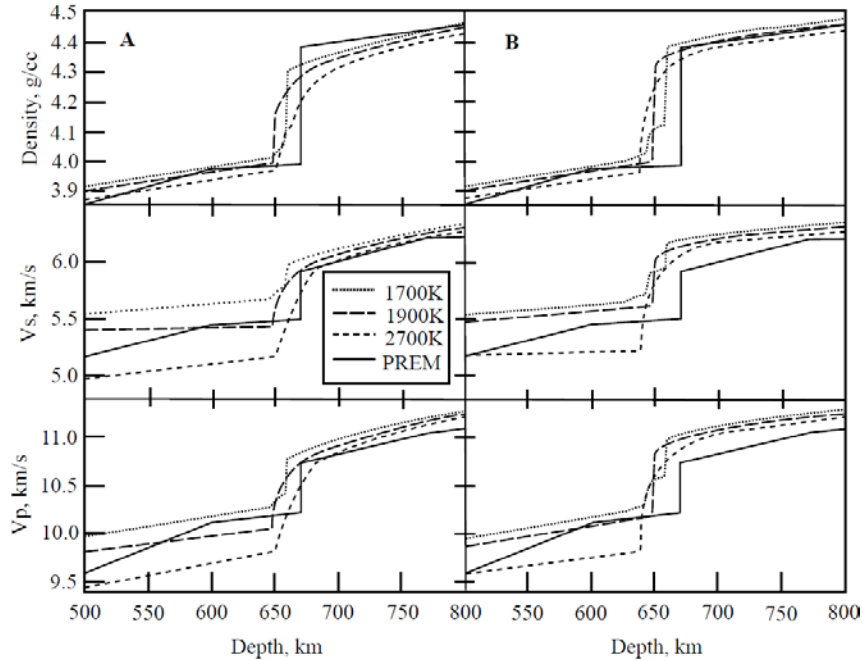


Figure 1.2: Calculated density and elastic wave velocities for different geotherms for pyrolite-like compositions with (a) 3% Al₂O₃ and (b) 5% Al₂O₃. Calculations are compared with the PREM seismological model (Dziewonski & Anderson 1981). Reproduced from Weidner & Wang 1998.

At subduction regions, a large-scale depression of the 660-km discontinuity is observed (Shearer & Masters 1992; Flanagan & Shearer 1998; Li & Yuan 2003). However, recent high-resolution studies present a more complicated structure characterized by multiple velocity variations (Niu & Kawakatsu 1996; Ai *et al.* 2003; Andrews & Deuss 2008; Wang & Niu, 2011) rather than a simply depressed discontinuity.

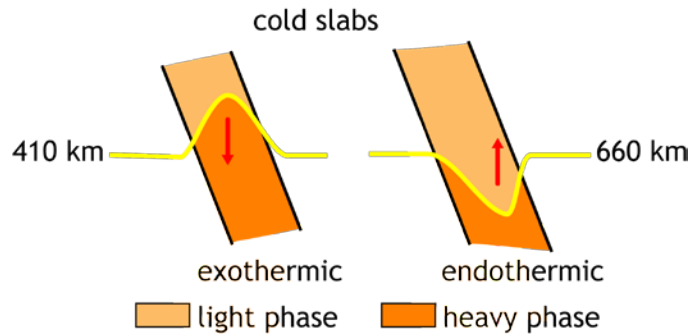


Figure 1.3: Cartoon showing the possible behaviour of seismic discontinuities in the transition when interacting with a subducting slab. Modified from Christensen (1995).

High-pressure laboratory experiments show that the $\alpha \rightarrow \beta$ and $\gamma \rightarrow$ perovskite plus magnesiowüstite phase transitions are positive and negative, respectively. That is, the 410-km discontinuity indicates an exothermic phase transition with a positive Clapeyron slope which at a subduction region represents a rise of the discontinuity due to the thermochemical properties of the mantle mineral phases at this depth. Conversely, the 660-km discontinuity represents an endothermic phase transition with a negative Clapeyron slope so a rise in temperature results in a decrease in pressure of the phase change. In other words, a depression of the 660-km discontinuity is expected at subduction zones where the cold slabs interact with the hotter surrounding mantle (Figure 1.3). This is in good agreement with seismological observations.

Many methods have been proposed to estimate the large-scale properties of mantle discontinuities (Shearer & Masters 1992; Lee & Grand 1996; Flanagan & Shearer 1998; Gu *et al.* 1998; Flanagan & Shearer 1999; Gu & Dziewonski 2002). These methods are complemented by high-resolution approaches such as

teleseismic receiver functions (Petersen *et al.* 1993; Kind *et al.* 1995; Sheehan 1995; Bostock 1996; Shen *et al.* 1996, 1998; Vinnik *et al.* 1996; Dueker & Sheehan 1997; Gurrola & Minster 1998; Li *et al.* 2000; Zhu & Kanamori 2000; Escalante *et al.* 2007) in regions well sampled by seismic stations. In this thesis, high-resolution sparse receiver functions are proposed and used to investigate the topography of the transition zone discontinuities beneath Japan and its geodynamical implications. The use of high quality data and a dense coverage of Ps converted phases guarantee the high-resolution image of the discontinuity topography and its interaction with the subducting slabs. The aim of this study is to strengthen our knowledge of the mantle transition zone through the introduction of an alternative and high-resolution approach (simultaneous iterative time-domain sparse deconvolution) for computing teleseismic receiver functions. Chapter 2 describes the complex tectonic circumstances of the Japanese islands as well as the present knowledge about the mantle transition zone beneath the study area. Chapter 3 introduces the sparse deconvolution as an alternative approach for computing receiver functions (sparse receiver functions). Chapter 4 shows the resulting high-resolution image of the mantle transition zone beneath Japan from sparse receiver functions. Chapter 5 summarizes the main results of the thesis.

1.2 References

- Ai, Y., Zheng, T., Xu, W., He, Y. & Dong, D., 2003. A complex 660 km discontinuity beneath northeast China, *Earth Planet. Sci. Let.*, **212**, 63-71.
- Akaogi, M., Tanaka, A. & Ito, E., 2002. Garnet-ilmenite-perovskite transitions in the system $\text{Mg}_4\text{Si}_4\text{O}_{12}$ - $\text{Mg}_3\text{Al}_2\text{Si}_3\text{O}_{12}$ at high pressures and high

- temperatures: phase equilibria, calorimetry and implications for mantle structure, *Phys. Earth Planet. Int.*, **132**, 303-324.
- Andrews, J. & Deuss, A., 2008. Detailed Nature of the 660 km region of the mantle from global receiver function data, *J. Geophys. Res.*, **113**, doi: 10.1029/2007JB005111.
- Bina, C.R. & Silver, P.G., 1990. Constraints on lower mantle composition and temperature from density and bulk sound velocity profiles, *Geophys. Res. Lett.*, **17**, 1153-1156.
- Bostock, M.G., 1996. *Ps* conversions from the upper mantle transition zone beneath the Canadian landmass, *J. geophys. Res.*, **101**, 8393–8402.
- Christensen, U., 1995. Effects of phase-transitions on mantle convection, *Annu. Rev. Earth Planet. Sci.*, **23**, 65-87.
- Dueker, K.G. & Sheehan, A.F., 1997. Mantle discontinuity structure from midpoint stacks of converted *P* to *S* waves across the Yellowstone hot spot track, *J. geophys. Res.*, **102**, 8313–8327.
- Duffy, T.S., Zha, C.S., Downs, R.T., Mao H.K. & Hemley, R.J., 1995. Elasticity of Forsterite to 16 Gpa and the composition of the upper-mantle, *Nature*, **378**, 170-173.
- Dziewonski, A.M. & Anderson, D.L., 1981. Preliminary reference earth model, *Phys. Earth Planet. Int.*, **25**, 297-356.
- Escalante, C., Gu, Y.J. & Sacchi, M., 2007. Simultaneous iterative time-domain sparse deconvolution to teleseismic receiver functions.
- Fei, Y., Mao, H. K. & Mysen, B. O., 1991. Experimental determination of element partitioning and calculation of phase-relations in the MgO-FeO-SiO₂ system at high-pressure and high-temperature, *J. Geophys. Res.*, **96**, 2157-2169.
- Flanagan, M.P. & Shearer, P.M., 1999. A map of topography on the 410-km discontinuity from *PP* precursors, *Geophys. Res. Lett.*, **26**, 549–552.
- Flanagan, M. P., & Shearer, P. M, 1998. Global mapping of topography on transition zone velocity discontinuities by stacking *SS* precursors, *J. Geophys. Res.*, **103**, 2673-2692.
- Frost, D.J., 2008. The upper mantle and transition zone, *Elements*, **4**, 171-176.

- Gu, Y.J. & Dziewonski, A.M., 2002. Global variability of transition zone thickness, *J. geophys. Res.*, **107**, doi:10.1029/2001JB000489.
- Gu, Y.J., Dziewonski, A.M. & Agee, C.B., 1998. Global de-correlation of the topography of transition zone discontinuities, *Earth Planet. Sci. Lett.*, **157**, 57–67.
- Gurrola, H. & Minster, J.B., 1998. Thickness estimates of the upper-mantle transition zone from bootstrapped velocity spectrum stacks of receiver functions, *Geophys. J. Int.*, **133**, 31–43.
- Helffrich, G. & Bina, C.R., 1994. Frequency-dependence of the visibility and depths of mantle seismic discontinuities, *Geophys. Res. Lett.*, **21**, 2613-2616.
- Kind, R., Kosarev, G.L. & Petersen, N.V., 1995. Receiver functions at the stations of the German Regional Seismic Network (GRSN), *Geophys. J. Int.*, **121**, 191–202.
- Lee, D.-K. & Grand, S., 1996. Depth of upper mantle discontinuities beneath the East Pacific Rise, *Geophys. Res. Lett.*, **23**, 3369–3372.
- Li, B.S., Liebermann, R.C. & Weidner, D.J., 1998. Elastic moduli of wadsleyite (beta-Mg₂SiO₄) to 7 gigapascals and 873 Kelvin, *Science*, **281**, 675-677.
- Li, X., Sobolev, S.V., Kind, R., Yuan, X. & Estabrook, Ch., 2000. A detailed receiver function image of the upper mantle discontinuities in the Japan subduction zone, *Earth Planet. Sci. Lett.*, **183**, 527–541.
- Li, X. & Yuan, X., 2003. Receiver functions in northeast China – implications for slab penetration into the lower mantle in northwest Pacific subduction zone, *Earth planet. Sci. Lett.*, **216**, 679-691.
- Liu, W., Kung, J. & Li, B.S., 2005. Elasticity of San Carlos olivine to 8 GPa and 1073 K, *Geophys. Res. Lett.*, **32**, L16301, doi:10.1029/2005GL023453.
- Niu, F. & Kawakatsu, H., 1996. Complex structure of the mantle discontinuities at the tip of the subducting slab beneath the northeast China: a preliminary investigation of broadband receiver functions, *J. Phys. Earth*, **44**, 701-711.
- Petersen, N., Vinnik, L.P., Kosarev, G., Kind, R., Oreshin, S. & Stammer, K., 1993. Sharpness of the mantle discontinuities, *Geophys. Res. Lett.*, **20**, 859–862.

- Oxburgh, E. R. & Turcotte, D.L., 1978. Mechanisms of continental drift, *Rep. Progress Phys.*, **41**, 1249-1312.
- Revenaugh, J. & Sipkin, S. A., 1994. Seismic evidence for silicate melt atop the 410 Km mantle discontinuity, *Nature*, **369**, 474-476.
- Ringwood, A.E. & Irifune, T., 1988. Nature of the 650-km seismic discontinuity - implications for mantle dynamics and differentiation, *Nature*, **331**, 131–136.
- Shearer, P.M., 2000. Upper mantle seismic discontinuity, in *Earth's Deep Interior: Mineral Physics and Tomography from the Atomic to the Global Scale*, AGU Geophysical Monograph, Vol. 117, 115–131.
- Shearer, P. M., & Masters, T. G., 1992. Global mapping of topography on the 660 km discontinuity, *Nature*, **355**, 791-796.
- Sheehan, A.F., Abers, G.A., Jones, C.H. & Lernerlam, A.L., 1995. Crustal thickness variations across the Colorado Rocky-Mountain from teleseismic receiver functions, *J. geophys. Res.*, **100**, 20 391–20 404.
- Shen, Y., Solomon, S.C., Bjarnason, I.T. & Purdy, G.M., 1996. Hot mantle transition zone beneath Iceland and the adjacent Mid-Atlantic Ridge inferred from *P*-to-*S* conversions and the 410- and 660-km discontinuities, *Geophys. Res. Lett.*, **23**, 3527–3530.
- Shen, Y., Sheehan, A.F., Dueker, K.G., de Groot-Hedlin, C. & Gilbert, H., 1998. Mantle discontinuity structure beneath the southern East Pacific Rise from *P*-to-*S* converted phases, *Science*, **280**, 1232–1235.
- Simmons, N.A. & Gurrola, H., 2000. Multiple seismic discontinuities near the base of the transition zone in the Earth's mantle, *Nature*, **405**, 559-562.
- Song, T. R. A., Helmberger, D. V. & Grand, S. P., 2004. Low-velocity zone atop the 410-km seismic discontinuity in the northwestern United States, *Nature*, **427**, 530-533.
- Stixrude, L., 2007. Properties of rocks and minerals – Seismic properties of rocks and minerals, and the structure of the Earth, in *Theatise on Geophysics*, Volume 2: Mineral Physics, G. Schubert, ed. Pp. 7-32, Oxford Elsevier Ltd., doi: 10.1016/B978-044452748-6/00042-0.

- Stixrude, L. & Lithgow-Bertelloni, C., 2005a. Mineralogy and elasticity of the oceanic upper mantle: Origin of the low-velocity zone, *J. Geophys. Res.*, **110**, B03204, doi: 10.1029/2004JB002965.
- Stixrude, L. & Lithgow-Bertelloni, C., 2005b. Thermodynamics of the mantle minerals: 1. Physical properties, *Geophys. J. Int.*, **162**, 610-632.
- Stixrude, L., 1997. Structure and sharpness of phase transitions and mantle discontinuities, *J. Geophys. Res.*, **102**, 14835-14852.
- Tonegawa, T., Hirahara, K., Sibutani, T., Iwamori, H., Kanamori, H. & Shiomi, K., 2008. Water flow to the mantle transition zone inferred from a receiver function image of the Pacific slab, *Earth Planet. Sci. Lett.*, **274**, 346-354.
- Tonegawa, T., Hirahara, K. & Shibutani, T., 2005. Detailed structure of the upper mantle discontinuities around the Japan subduction zone imaged by receiver function analyses, *Earth Planets Space*, **57**, 5-14.
- Vacher, P., Mocquet, A. & Sotin, C., 1998. Computation of seismic profiles for explaining the 660 km depth discontinuity, *Phys. Earth Planet. Inter.*, **106**, 275-298.
- Vinnik, L.P., Kosarev, G. & Petersen, N., 1996. Mantle transition zone beneath Eurasia, *Geophys. Res. Lett.*, **23**, 1485-1488.
- Wang, B. & Niu F., 2011. Spatial variations of the 660-km discontinuity in the western Pacific subduction zones observed from CEArray triplication data, *Earthq. Sci.*, **24**, 77-85.
- Weidner, D.J. & Wang, Y.B., 1998. Chemical- and Clapeyron-induced buoyancy at the 660 km discontinuity, *J. Geophys. Res.*, **103**, 7431-7441.
- Zha, C.S., Duffy, T.S., Mao, H.K., Downs R.T., Hemley, R.J. & Weidner, D.J., 1997. Single-crystal elasticity of beta-Mg₂SiO₄ to the pressure of the 410 km seismic discontinuity in the Earth's mantle, *Earth Planet. Sci. Lett.*, **147**, E9-E15.
- Zhu, L. & Kanamori, H., 2000. Moho depth variation in Southern California from teleseismic receiver functions, *J. Geophys. Res.*, **105**, 2969-2980.

CHAPTER 2

JAPAN SUBDUCTION ZONE AND TECTONIC SETTING

2.1 Introduction

Japan is perhaps one of the best monitored places in the world, with extensive geophysical and geological observatory networks distributed over the whole Japanese island arcs. It is also known for its significant structural complexity associated with active subduction processes and crustal deformation. Over the last decades, many efforts have been made to obtain a complete and detailed picture of the geological history and the profound dynamical implications. Although such a goal has not been achieved yet, the Japanese arc system is better understood than any other arc system in the world (Taira 2001).

Seismologically, Japan has been extensively investigated not only because it is densely and uniformly covered by high quality seismic networks (e.g. F-NET broadband seismograph network) but also for its high seismicity related to subducting plates and several subsurface processes and structures. This makes it possible to image the crust and upper-mantle structure beneath Japan with high resolution (Zhao *et al.* 1992, 2007, 2009; 2011). However, there are still many intriguing problems and active debates regarding several geological and geophysical observations related, for instance, to mantle heterogeneity and dynamics, the structure and fate of the subducting slabs, among many others. In this chapter, a brief overview of the tectonic setting and subduction processes of

the Japanese island arc system, as well as its mantle structure and dynamics is presented.

2.2 Tectonic Setting

Japan is mainly composed of four islands: Hokkaido, Honshu, Shikoku, and Kyushu (Figure 2.1b). Most of its geology is the result of subduction-related processes since the Mesozoic (Sugimura & Uyeda 1973) and is characterized by complex tectonic structure and geologic history. These processes are responsible for the active seismicity and volcanism in and around the Japan.

The Japanese islands lie at the junction of five major tectonic plates (Figure 2.1a,c): the Pacific and Philippine Sea oceanic plates and the North America (or Okhotsk), Eurasian and Amurian continental plates (Taira 2001). Based on dense geodetic observations (Sagiya *et al.* 2000) as well as the seismicity and patterns of active faulting (Research Group of Active Faults in Japan 1991), it has been possible to obtain a clear and detailed picture of where tectonic motions occur (Figure 2.2). The observations indicate that the active tectonics of northeast Japan (northern Honshu and Hokkaido) are the manifestation of the interaction between the Amur and Okhotsk subplates with the Pacific plate which is dominated by mostly westward motions ranging from 3 to 5 cm/year and represent deformations produced by the subduction of the Pacific plate (Taira 2001). To the southwest (Shikoku and southwest Honshu), the Philippine Sea plate moves towards the NW at a rate of approximate 5 cm/year (Wei & Seno 1998) and subducts beneath SW Japan and the Ryukyu arc. The active tectonics, observed in this region, is

produced from the interaction of the Philippine Sea plate and Amur subplate (Seno 1977; Taira 2001) and is characterized by WNW motions that range from 2 to 3 cm/year (Taira 2001). In this region, the volcanic front lies parallel to the Ryukyu trench and the Nankai Trough. However, it becomes less significant in Central Honshu and in Shikoku, as the depth of the subducting Philippine Sea plate is less than 100 km which is shallower than the depth of the partial melting (Wei & Seno 1998). From southern Kyushu to the Ryukyu arc, the tectonic motions are mainly SE, in contrast with the rest of the Japanese arc system and might represent the effect of back-arc basin rifting of the Okinawa trough (Taira 2001).

There are various interpretations of the boundaries of the Okhotsk and the Amur subplates. Geodetic, seismic and geological observations suggest that these boundaries run from Sakhalin, via the eastern margin of the Japan Sea, to the Itoigawa-Shizuoka Tectonic Line which divides the Japanese island arc into NE and SW Japan arcs (Nakamura 1983; Seno *et al.* 1996). At this location, an eastward motion of the Amur subplate is suggested as the subduction of the Pacific and Philippine Sea plates alone cannot fully explain the E-W compression at the plate boundary. The tectonic setting is also complicated by the triple junction between the Okhotsk, Amur and Philippine Sea plates.

In terms of tectonic evolution, Japan has been in a zone of subduction since the Permo-Jurassic (>295-135 Ma), when it lay on the eastern edge of the Gondwanaland (Saito & Hashimoto 1982). Accretion has continued since then, on the western margin of the Panthalassa (Isozaki 1998) and then Pacific Oceans,

with wedges of oceanic sediments and underlying oceanic crust basalts being detached from the subducting oceanic plate and accreted to the fore-arc zone of the continental plate to the west (Taira 2001). The crust of the Japanese islands has thus grown progressively from the west (Asian continental side), with the rocks becoming younger towards the Pacific side. Crustal thinning by accretion was associated with granite formation, especially during the Cretaceous (135-65 Ma). Subsequently, the basement rocks of the islands comprise largely Mesozoic to Palaeogene accretionary wedges, with the older rocks intruded by Cretaceous and Tertiary granites (Figure 2.3).

Development of the current outline of the Japanese islands largely took place during the period between 20 Ma and 15-14 Ma, concurrent with the spreading of the Japan Sea. The present rate and pattern of movement of the major plates were established around 2 Ma.

In summary, Figure 2.3 displays a paleogeographic reconstruction since 130 Ma. A more detailed time sequence evolution can also be found in Taira (2001).

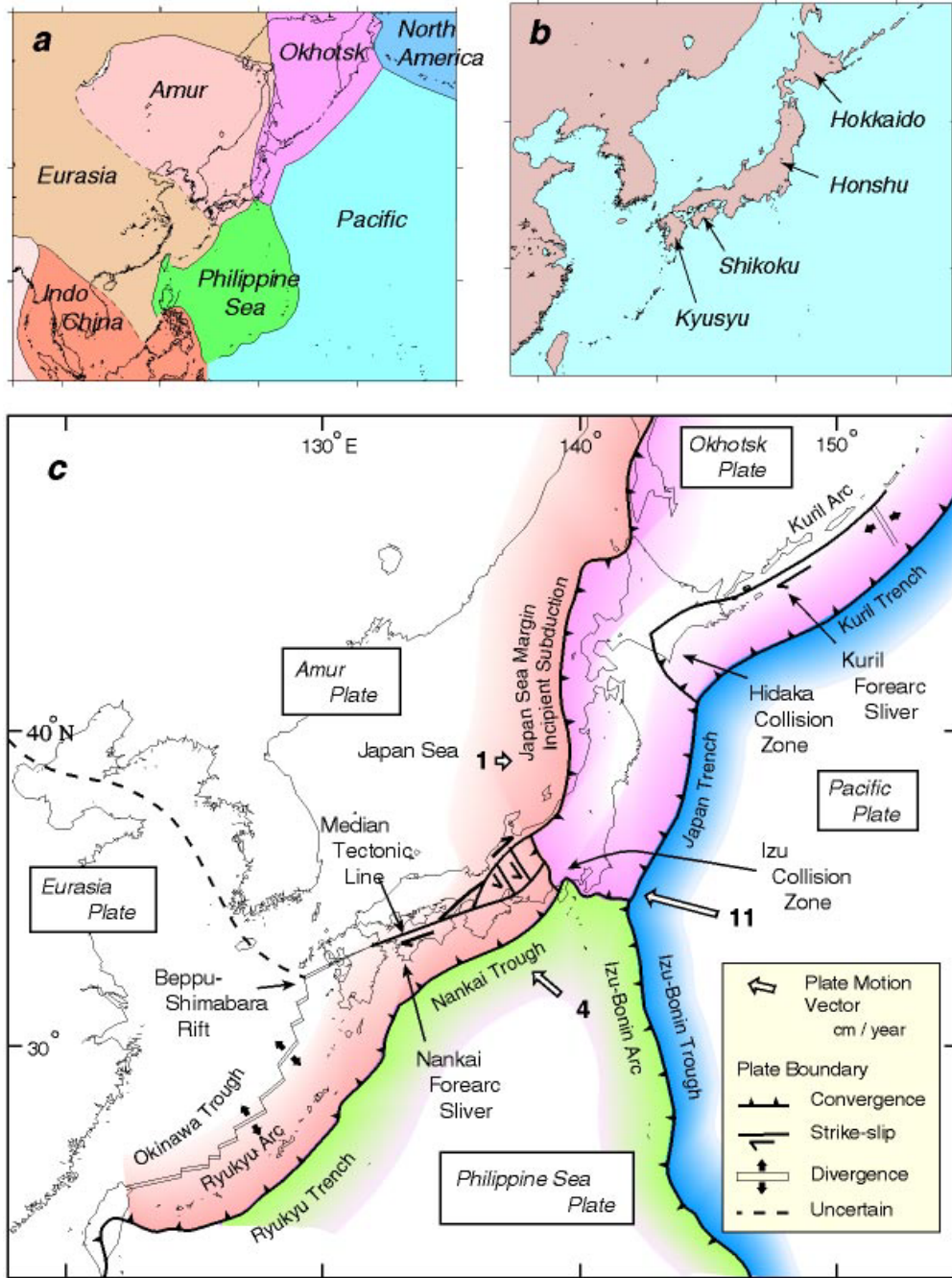


Figure 2.1: Plate tectonics of the Japanese arc system. (a) Plate tectonic framework of Northeastern Asia (modified after Wei & Seno 1998). (b) Main part of the Japanese arc system, showing the distribution of the four big islands. (c) Plate boundaries of the Japanese arc system. Note that central Honshu shows complex microplate tectonics dominated by the median tectonic line (MTL), right-lateral motion, and bookshelf-type rotation tectonics (from Taira 2001).

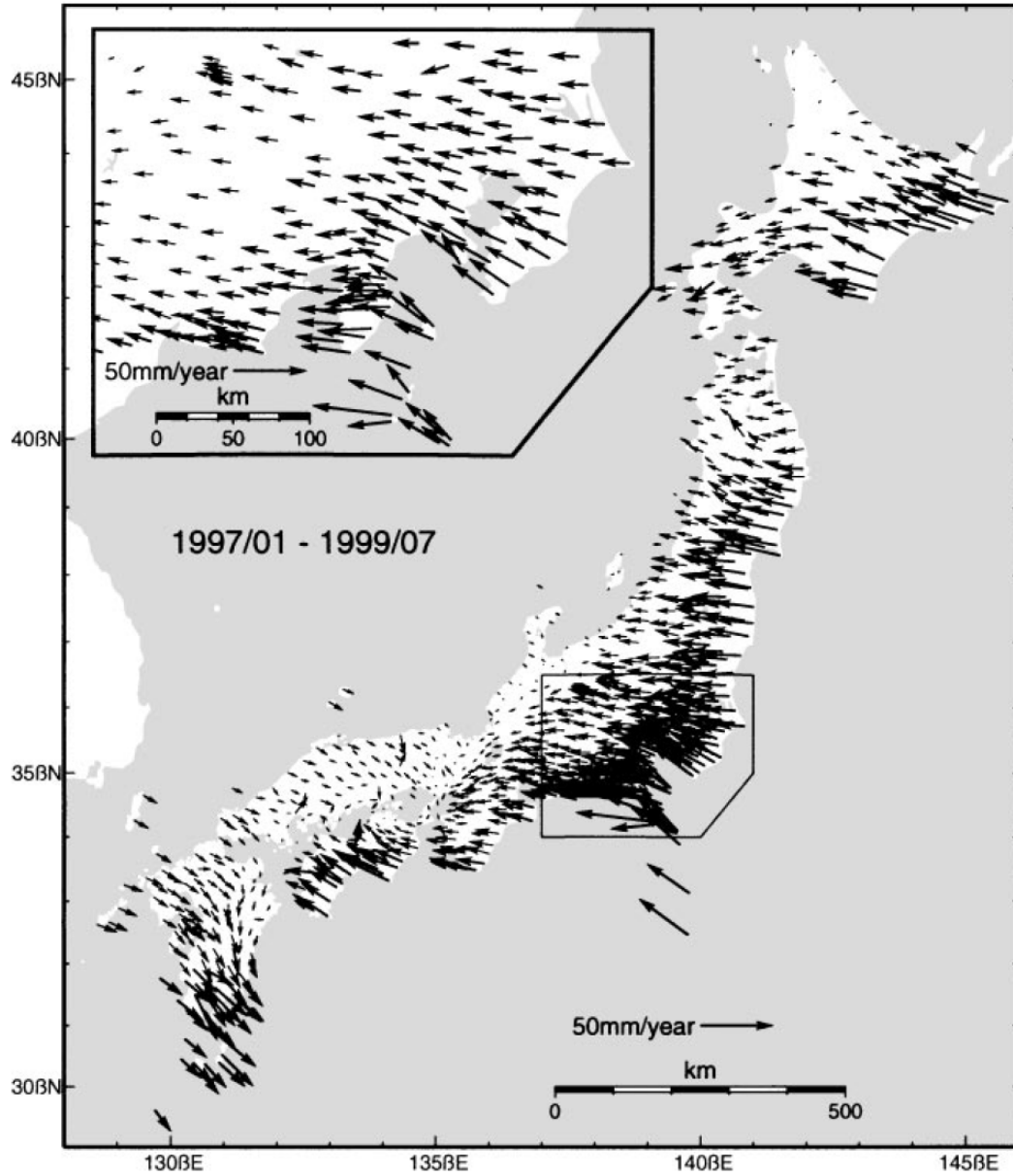


Figure 2.2: GPS vector data (1997 - 1999) from GEONET, the GPS network maintained by the Geography Survey Institute of Japan, showing crustal deformation of the Japanese arc system (after Sagiya *et al.* 2000). Modified from Taira 2001.

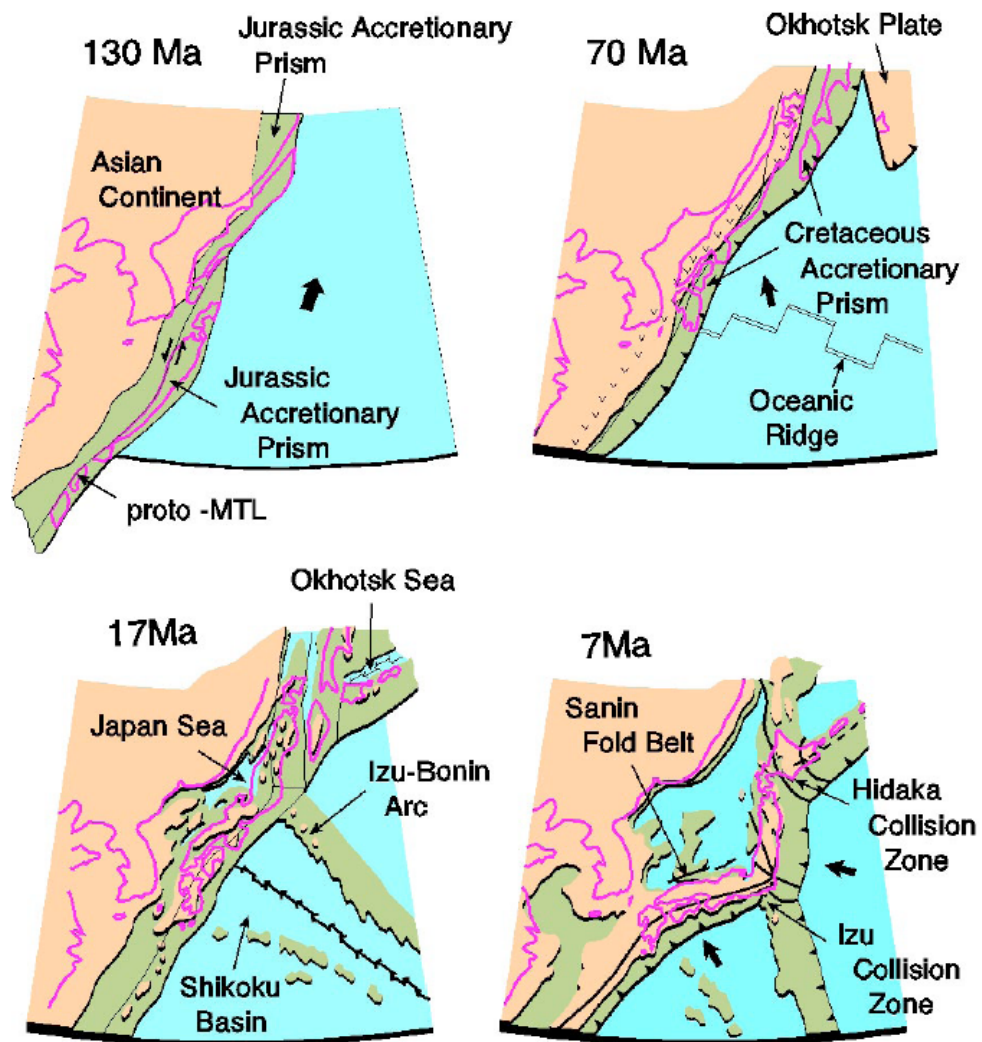


Figure 2.3: Paleogeographic reconstruction since 103 Ma (after Taira *et al.* 1989).
Reproduced from Taira 2001.

2.3 Japanese Subduction Zone

The mantle structure under Japan is perhaps the best resolved on Earth through a variety of observations including careful relocation of earthquake hypocenters, petrology, seismic tomography, shear-wave splitting, attenuation, gravity, topography, geochemistry, etc. It is clear that there exists significant 3D structure and complexity within the region's subduction zones. Examples include change in dip along the arcs and also many forms of slab deformation and distortions of phase and chemical boundaries due to geochemical transformations and reactions.

Several tomographic studies have been performed to investigate the 3D velocity, geometry, and attenuation structures beneath Japan (Hirahara, 1981, Zhao *et al.* 1992, 1994, 2000, 2009; Zhao & Hasegawa 1993; Tsumura *et al.* 2000; Nakajima *et al.* 2001; Salah & Zhao 2003; Wang and Zhao 2005). Results of a recent local tomography study of the Japan subduction zone (Zhao *et al.* 2009) is shown in Figure 2.4. In this figure, the subducting Pacific slab is clearly imaged as a high velocity anomaly which is ~85 km thick and has *P* and *S* wave velocities 3-6% faster than the surrounding mantle. Low velocities and high Poisson's ratio anomalies represent the source zone of arc magmatism and volcanism caused by the slab dehydration and corner flow in the mantle wedge (Deal & Nolet 1999; Zhao *et al.* 2011).

Although tomographic studies play an increasingly important role in understanding slab structure, they do not provide information about the stress regime and many other important parameters to better constrain mantle structure

and dynamics. For this reason, many other methods have been used to fill the gaps regarding, for example, mantle structure, mineral physics, phase changes, fate of slabs, mantle discontinuities and, water in the mantle.

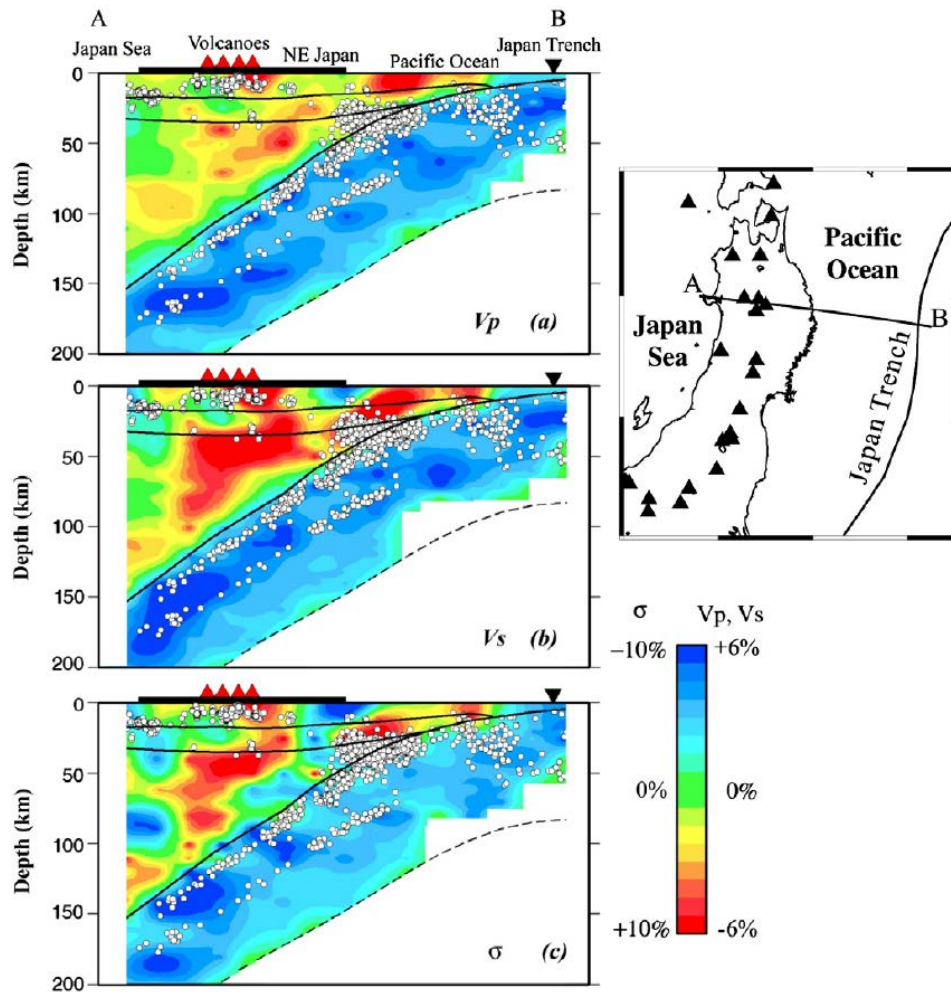


Figure 2.4: Vertical cross-section of (a) P -wave velocity, (b) S -wave velocity, and (c) Poisson's ratio perturbations along a profile as shown in the inset map (Zhao *et al.* 2009, 2011). Red denotes low velocity and high Poisson's ratio, while blue denotes high velocity and low Poisson's ratio. Red triangles denote active arc volcanoes. The reverse triangles show the location of the Japan Trench. Small white dots shown earthquakes which occurred within a 15-km width along the profile. The curved lines show the Conrad and Moho discontinuities and the upper boundary of the subducting Pacific slab. The dashed lines denote the estimated low boundary of the Pacific slab.

One of the most challenging tasks, facing observational seismologists, is to map the topography of the transition zone discontinuities in a subduction system. In the Japan subduction zone, many techniques have been used, from global to local observations, to achieve this task. However, the results seem to agree and disagree in many instances. For instance, from *Ps* converted phases, a normal 410-km discontinuity was found where the slab directly reaches this depth. The 660-km discontinuity, however, shows a depression down to 700 km depth at places where it traverses the slab (Li *et al.* 2000). This is contrary to tomographic studies that show a flat lying slab on the 660-km discontinuity (Bijwaard *et al.* 1998). Similarly, ScS reverberations (Kato *et al.* 2001) show a 660-km discontinuity depressed by about 10 km and no significant structure at the 410-km discontinuity. Near-vertical reflections from regional earthquakes (Tono *et al.* 2005) recorded by more than 500 tiltmeters in Japan show a 660-km discontinuity depressed by 15 km and an elevated 410-km discontinuity within the subducting slab. Comparable results are obtained by Tonegawa *et al.* 2005, 2008 using receiver functions (~50 km depression of the 660-km discontinuity and an elevation of ~30 km of the 410-km discontinuity).

In general, it appears that the 660-km discontinuity is depressed by approximately 50 km at the Japanese subduction zone while the 410-km discontinuity remains unclear or shows no obvious topographic variation (Kind & Li, 2007).

The sharpness of the transition zone discontinuities is also another intriguing problem as some studies show discontinuity thickness of up to ~50 km for the 410- and 660-km discontinuities (Yamazaki & Hirahara 1994) while others

identify a sharp 660-km discontinuity and variable 410-km discontinuity (Tonegawa *et al.* 2005; Lebedev *et al.* 2002). Moreover, a 520-km discontinuity is clearly observed in some regions but not identified in many others. What is clear is that even though many of these studies show certain agreement, more detailed studies and better approaches are needed to map the topography of these discontinuities and to interpret them in terms of subduction dynamics.

Estimating seismic anisotropy is another challenging problem. Seismic anisotropy is assumed to be the result of lattice preferred orientation of mantle minerals such as olivine (Zhang & Karoto, 1995). However, recent laboratory experiments suggest that the olivine slip system changes under high stress in hydrated systems, which is the case in subduction zones (Jung & Karoto, 2001). This makes it even more difficult to explain the shear-wave splitting results. In the Japan subduction zone many shear-wave splitting observations indicate a range of preferred orientation from trench-parallel near the trench to convergence-parallel in the back-arc. This diversity of orientations likely arises from the complexity of the subduction system, with two triple junctions and multiple subducting slabs as well as crustal deformation (Hiramatsu & Ando 1996; Fouch & Fischer 1996; Long & van der Hilst 2005). Under Hokkaido island, splitting variations are consistent with NS shear in the overriding plate or the presence of hydrated mantle wedge (Nakijima & Hasegawa 2004). To the south at Honshu and Ryukyu island, shear-wave splitting directions range from trench-parallel near the trench to trench-orthogonal into the back-arc (Fouch & Fischer 1996; Long & van der Hilst 2005). In general, in the Japan subduction zone shear-wave splitting results are consistent

with a hydrated wedge; however, many other modeling alternatives are also possible (Kneller *et al.* 2005, King 2007).

In the last few years, many efforts have been made to understand the variations in seismic velocity near subducting slabs, as they might provide constraints about the thermal structure and the distributions of hydrous minerals and water in a subduction zone. It is through subducted slabs that oceanic crust and sediments, including volatile compounds such as water are recycled back into the mantle. In a recent tomography study, Abdelwahed & Zhao 2007 identified significant low-velocity anomalies in deep portions of the mantle wedge above the Pacific slab which could be caused by the deep dehydration process of the old Pacific slab consistent with mineral physics results. Similar results were obtained from a high-resolution receiver function analysis by Tonegawa *et al.* 2008 showing seismic velocity contrast of up to 8%. Furthermore numerical simulations suggest that the hydrated minerals are stable at the base of the mantle wedge, at least down to the 410-km discontinuity.

Electrical conductivity models show clear high conductivity anomalies beneath the northern Japan and its vicinity in the transition zone (Shimizu *et al.* 2010; Fukao *et al.* 2004). The results suggest that the conductivity anomaly extends down to the bottom of the mantle transition zone followed with a weak resistivity anomaly which is likely produced by temperature effects and/or the presence of large amount of water, similar to anomalies observed in Hawaii (Shimizu *et al.*, 2010). In general, lower temperatures and higher water content anomalies are observed in SW Japan. Conversely, higher temperatures and lower water content

anomalies are observed in NE Japan. These water content variations correlate with spatial variations in composition at the bottom of the mantle transition zone (Yamada *et al.* 2009).

2.4 References

- Abdelwahed, M. & Zhao, D., 2007. Deep structure of the Japan subduction zone. *Phys.Earth Planet. Inter.*, **162**, 32–52.
- Bijwaard, H., Spakmam, W. & Engdahl, E.R., 1998. Closing the gap between regional and global travel time tomography, *J. Geophys. Res.*, **103**, 30055–30078.
- Deal, M.M. & Nolet, G., 1999. Slab temperature and thickness from seismic tomography. Part 2: Izu-Bonin, Japan, and Kuril subduction zones. *J. Geophys. Res.*, **104**, 28803–28812.
- Fouch, M.J. & Fischer, K.M., 1996. Mantle anisotropy beneath northwest Pacific subduction zones. *J. Geophys. Res.*, **101**, 15987–16002.
- Isozaki, Y., 1997. Constraining two types of orogen in Permo-Triassic Japan: accretionary versus collisional *Isl. Arc*, **6**, 2-24.
- Jung, H. & Karato, S., 2001. Water-induced fabric transitions in olivine. *Science*, **293**, 1460–1463.
- Kato, M., Misawa, M. & Kawakatsu, H., 2001. Small subsidence of the 660-km discontinuity beneath Japan probed by ScS reverberations. *Geophys. Res. Lett.*, **28**, 447–450.
- Kneller, E.A., van Keken, P.E., Karato, S. & Park, J., 2005. B-type olivine fabric in the mantle wedge; insights more high resolution non-Newtonian subduction models. *Earth Planet. Sci. Lett.*, **237**, 781–797.
- Lebedev, S., Chevrot, S. & van der Hilst, R.D., 2002. The 660-km discontinuity within the subducting NW-Pacific lithospheric slab, *Earth Planet. Sci. Lett.*, **205**, 25–35.

- Li, X., Sobolev, S.V., Kind, R., Yuan, X. & Estabrook, C.H., 2000. A detailed receiver function image of the upper mantle discontinuities in the Japan subduction zone, *Earth Planet. Sci. Let.*, **183**, 527–541.
- Long, M.D. & van der Hilst, R.D., 2005. Upper mantle anisotropy beneath Japan from shear wave splitting. *Phys. Earth Planet. Int.*, **151**, 206–222.
- Nakajima, J. & Hasegawa, A., 2004. Shear-wave polarization anisotropy and subduction-induced flow in the mantle wedge of northeastern Japan. *Earth Planet. Sci. Let.*, **225**, 365–377.
- Nakajima, J., Tsuji, Y., Hasegawa, A., Kita, S., Okada, T. & Matsuzawa, T., 2009. Tomographic imaging of hydrated crust and mantle in the subducting Pacific slab beneath Hokkaido, Japan: evidence for dehydration embrittlement as a cause of intraslab earthquakes, *Gondwana Res.*, **16**, 470–481.
- Nakamura, K., 1983. Possible nascent trench along the eastern Japan Sea as the convergent boundary between Euroasian and North American plates, *Bull. Earthq. Res. Inst., Univ. Tokyo*, **58**, 711-722.
- Research Group for Active Faults in Japan, 1991. *Active Faults in Japan, Sheet Maps and Inventories*. Tokyo: Univ. Tokyo Press. 437 pp. (in Japanese)
- Sagiya, T., Miyazaki, S. & Tada, T., 2000. Continuous GPS array and present-day crustal deformation of Japan, *Pure Appl. Geophys.*, **157**, 2303-2322.
- Saito, Y. & Hashimoto, M., 1982. South Kitakami region: an allochthonous terrane in Japan, *J. Geophys. Res.*, **87**, 3691-3696.
- Salah, M. & Zhao, D., 2003. 3-D seismic structure of Kii Peninsula in southwest Japan: evidence for slab dehydration in the forearc, *Tectonophysics*, **364**, 191–213.
- Seno, T., Sakurai, T. & Stein, S., 1996. Can the Okhotsk plate be discriminated from the North American plate?, *J. Geophys. Res.*, **101**, 11305-11315.
- Seno, T., 1977. The instantaneous rotation vector of the Philippine Sea plate relative to the Euroasian plate, *Tectonophysics*, **42**, 209-226.
- Sugimura, A. & Uyeda, S., 1973. Island Arc – Japan and its Environs, Elsevier, Amsterdam, 247 pp.

- Taira, A., 2001. Tectonic evolution of the Japanese island arc system, *Annu. Rev. Earth Planet. Sci.*, **29**, 109-134.
- Taira, A., Tokuyama, H. & Soh, W., 1989. Accretion tectonics and evolution of Japan. In *The evolution of the Pacific Ocean Margins*, Oxford Monogr. Geol. Geophys., ed. Z Ben-Avrham, **8**, 100-123. Oxford, UK, Oxford Univ. Press 234 pp.
- Tonegawa T., Hirahara K. & Shibutani, T., 2005. Detailed structure of the upper mantle discontinuities around the Japan subduction zone imaged by receiver function analyses, *Earth Planets and Space*, **57**, 5–14.
- Tono, Y., Kunugi, T., Fukao, Y., Tsuboi, S., Kanjo, K. & Kasahara, K., 2005. Mapping of the 410- and 660-km discontinuities beneath the Japanese islands, *J. Geophys. Res.*, **110**, 1–10.
- Wei, D. & Seno, T., 1998. Determination of the Amurian plate, in *Mantle Dynamics and Plate Interactions in East Asia*, Geodyn. Ser., ed. SL Flower, C Chung, T Lee, **27**, 337-346. Washington, DC: Am. Geophys. Union. 419 pp.
- Yamazaki, A. & Hirahara, K., 1994 The thickness of upper mantle discontinuities, as inferred from short-period J-Array data, *Geophys. Res. Let.*, **21**, 1811–1814.
- Zhang, S. & Karoto, S., 1995. Lattice preferred orientation of olivine aggregates deformed in simple shear, *Nature*, **375**, 774-777.
- Zhao, D., Yu, S. & Ohtani, E., 2011. East Asia: Seismotectonics, magmatism and mantle dynamics, *J. Asian Earth Sci.*, **40**, 689-709.
- Zhao, D., Wang, Z., Umino, M. & Hasegawa, A., 2009. Mapping the mantle wedge and intraplate thrust zone of the northeast Japan arc, *Tectonophysics*, **467**, 89-106.
- Zhao, D., Maruyama, S & Omori, S., 2007. Mantle dynamics of western Pacific to East Asia: New insights from seismic tomography and mineral physics, *Gondwana Res.*, **11**, 120-131.
- Zhao, D., Ochi, F., Hasegawa, A. & Yamamoto, A., 2000. Evidence for the location and cause of large crustal earthquakes in Japan, *J. Geophys. Res.*, **105**, 13579–13594.

Zhao, D., Hasegawa, A. & Kanamori, H., 1994. Deep structure of Japan subduction zone as derived from local, regional and teleseismic events, *J. Geophys. Res.*, **99**, 22313–22329.

Zhao, D., Hasegawa, A. & Horiuchi, S., 1992. Tomographic imaging of *P* and *S* wave velocity structure beneath northeastern Japan, *J. Geophys. Res.*, **97**, 19909-19928.

CHAPTER 3

SIMULTANEOUS ITERATIVE TIME-DOMAIN SPARSE DECONVOLUTION TO TELESEISMIC RECEIVER FUNCTIONS¹

3.1 Introduction

Crustal and mantle discontinuities play an important role in characterizing major changes in seismic velocity, rheology, and potentially chemical composition (Ringwood & Irifune 1988; Stixrude 1997; Shearer 2000). In recent years, several methods have been proposed to estimate large-scale properties of discontinuities (Shearer & Masters 1992; Lee & Grand 1996; Flanagan & Shearer 1998; Gu *et al.* 1998; Flanagan & Shearer 1999; Gu & Dziewonski 2002). These methods are complemented by high-resolution approaches such as teleseismic receiver functions (Petersen *et al.* 1993; Kind *et al.* 1995; Sheehan 1995; Bostock 1996; Shen *et al.* 1996, 1998; Vinnik *et al.* 1996; Dueker & Sheehan 1997; Gurrola & Minster 1998; Li *et al.* 2000; Zhu & Kanamori 2000) in regions well sampled by seismic stations. Receiver functions are time series representing *P*-to-*S* conversions of teleseismic waves at discontinuities in response to the earth structure beneath the receiver. Assuming nearly horizontal layers, most of the converted energy is observed in the radial and traverse components. By deconvolving the horizontal component with the vertical component, the influence of the source and near source structure can be effectively removed. In

¹ A version of this chapter has been published. Escalante *et al.* 2007. *Geophysical Journal International*. 171: 316-325.

other words, the vertical component is used as an effective source time function to isolate the local response from the horizontal component (Langston 1977, 1979, 1981; Owens & Crosson 1988; Ammon *et al.* 1990; Ammon 1991).

One of the most commonly used techniques to compute receiver functions is frequency-domain deconvolution (Clayton & Wiggins 1976; Bostock 1996; Dueker & Sheehan 1997; Shu & Kanamori 2000; Lawrence & Shearer 2006), also called water-level deconvolution. This method performs a spectral division between the horizontal component (either radial or traverse) and the vertical component (source spectrum) and uses a water-level stabilizer to avoid the amplification of small spectral components. Another approach is time-domain deconvolution (Oldenburg 1981; Abers *et al.* 1995; Gurrola *et al.* 1995; Yuan *et al.* 1997; Zhu 2004) that can be solved using the method of least squares. In this case, a trade-off parameter is used to stabilize the inversion. These two approaches generally produce similar results when the available data are broadband with high signal-to-noise ratio (Ligarría & Ammon 1999).

In reality, seismic data often contain substantial noise, especially when the source is relatively weak and/or the structural complexity is high. Therefore, successful applications of a given method often depend on its effectiveness in removing the noise and enhancing the desirable features of the signal. For this reason, several deconvolution approaches have been proposed in seismic and ultrasonic applications (Pham & de Figueiredo 1989; Mendel 1990; Sacchi 1997; Olofsson 2004). These methods attempt to construct a high-resolution solution to the deconvolution problem by imposing sparsity on the unknown reflectivity model.

In this paper, we adopt the technique proposed by Sacchi (1997) for the deconvolution of seismic events in reflection seismology. The method consists of solving the deconvolution inverse problem with a regularization strategy based on a Cauchy criterion. The latter is used to retrieve sparse reflectivity sequences. The term “sparse” is used to refer to a solution that contains a few non-zero samples (reflectors). It is important to mention that results similar to the ones found in this paper could be obtained using the so-called minimalist receiver functions proposed by Menke (personal communication, 2007). Minimalist receiver functions are found via a non-linear optimization method where one needs to estimate the arrival times and amplitudes for an assumed number of spikes. This method produces models that consists of a minimal number of pulses needed to fit the observations within a desired level of accuracy (see also Menke & Levin 2004 for its application to SKS splitting).

The main objective of this paper is to introduce an iterative time-domain sparse deconvolution method for computing teleseismic receiver functions. This method was applied to both synthetic and actual seismic data recorded at station ABU, Japan. Our results clearly demonstrate that the sparse deconvolution approach is a simple, efficient and high-resolution alternative to the existing methods.

3.2 Sparse Deconvolution

Receiver function determination is inherently a deconvolution problem. The solutions obtained by common techniques, such as water-level based spectral division (e.g. Ammon 1991) and time-domain deconvolution (e.g. Gurrola *et al.*

1995), can be equally effective when using sufficiently broad-band records with good signal-to-noise levels. Unfortunately, in most of the cases, the band-limitation of data leads to suboptimal deconvolution results. Hence, the choice of an appropriate deconvolution technique is vital.

A sparse deconvolution problem is usually referred to: given some observation sequence $\mathbf{R} = \{R_1, \dots, R_M\}$, find the sparse signal $\mathbf{r} = \{r_1, \dots, r_N\}$ such that

$$\mathbf{R} = \mathbf{Z}\mathbf{r} + \mathbf{n}, \quad (3.1)$$

where \mathbf{Z} is a convolution matrix and \mathbf{n} represents the noise. The signal \mathbf{r} is known to be sparse, that is, only a few of its samples have non-zero values.

In theory, a solution of \mathbf{r} that minimizes the squared error $E^2 = \|\mathbf{R} - \mathbf{Z}\mathbf{r}\|_2^2$ can be easily found if \mathbf{Z} is known. In practice, however, a stable solution cannot be uniquely determined due to the ill-conditioned character of \mathbf{Z} (typically band-limited). A generic approach to overcome this problem is to apply regularization techniques by including some *a priori* knowledge of the solution.

Sacchi (1997) used different reweighting strategies to improve the deconvolution of seismic records and retrieved sparse reflectivity sequences by applying a Cauchy criterion. This criterion is derived by considering that the unknown reflectivity can be modeled via a Cauchy distribution (Figure 3.1). The latter is a long-tail probability distribution that is commonly used as a priori for the inversion of sparse models and signals. Due to its narrower peak, most of the

solution following the long-tailed distribution will be zero values while the non-zero values will have a bigger range of amplitudes (i.e., a sparse solution).

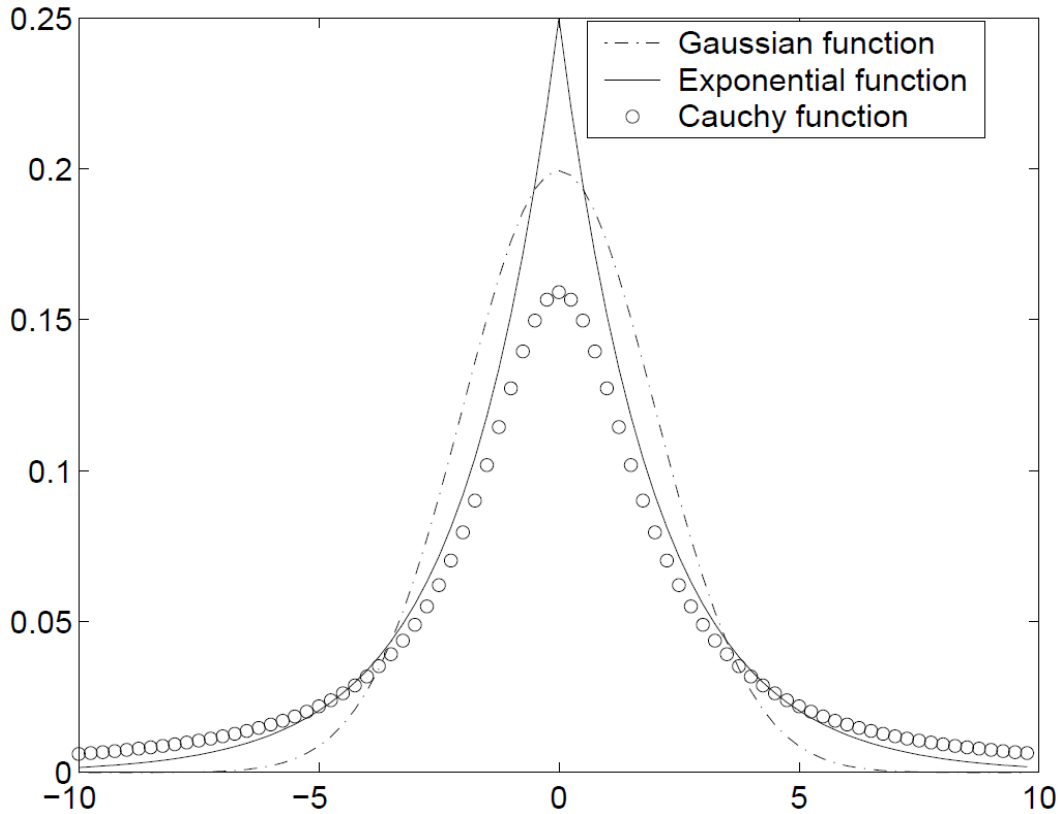


Figure 3.1: Probability distributions for Gaussian, exponential, and Cauchy functions that have a mean value of 0, and a variance value of 4.

In time-domain, the deconvolution can be achieved by solving the convolution equation:

$$\mathbf{Z}(t) * r(t) = \mathbf{R}(t), \quad (3.2)$$

which can be solved using a least-squares approach. For an ideal case, we can rewrite this equation in matrix form as (Gurrola *et al.* 1995)

$$\mathbf{R} = \mathbf{Zr}, \quad (3.3)$$

where \mathbf{R} can be either the radial or traverse component and contains M elements, \mathbf{r} is the receiver function composed of N elements, and \mathbf{Z} is the convolution matrix created by the vertical component (z) of the seismogram of k elements. In other words, each column of \mathbf{Z} contains a vector \mathbf{z} properly padded with zeros. The size of \mathbf{Z} is $N \times M$ as follows:

$$\mathbf{Z} = \begin{pmatrix} z_1 & 0 & \vdots & \vdots & \cdots & 0 \\ \vdots & z_1 & 0 & \vdots & \vdots & \vdots \\ z_k & \vdots & z_1 & \ddots & \vdots & \vdots \\ 0 & z_k & \vdots & \ddots & \vdots & \vdots \\ \vdots & 0 & z_k & \vdots & z_1 & 0 \\ \vdots & \vdots & 0 & \ddots & \vdots & z_1 \\ \vdots & \vdots & \vdots & \vdots & z_k & \vdots \\ \vdots & \vdots & \vdots & \vdots & 0 & z_k \end{pmatrix}. \quad (3.4)$$

According to Gurrola *et al.* (1995), in a noise-free case we can solve equation (3.3) directly for the receiver function, which in principle should produce a result similar to the water-level deconvolution. In reality \mathbf{R} contains noise, therefore, an exact solution to (3.3) would introduce noise into our results due to overfitting the data. Here, we are looking for a solution in which the difference between the observations \mathbf{R} and predicted \mathbf{Zr} is minimized. A solution to this problem can be expressed as

$$\mathbf{r} = (\lambda \mathbf{I} + \mathbf{Z}^T \mathbf{Z})^{-1} \mathbf{Z}^T \mathbf{R}, \quad (3.5)$$

where \mathbf{I} is an $N \times N$ identity matrix, and λ is a trade-off parameter. The appropriate value for λ would be one that satisfies equation (3.3) within a tolerance level.

This method, as well as frequency-domain method, are both examples of a damped least-squares deconvolution (Gurrola *et al.* 1995). In either case, we test a range of water-level values or λ to obtain an optimal deconvolution result.

The sparse constraint can be implemented by minimizing the following cost function:

$$\mathbf{J} = \|\mathbf{Z}\mathbf{r} - \mathbf{R}\|_2^2 + \mu \sum_{i=1} \ln(1 + ar_i^2), \quad (3.6)$$

where the second term on the right-hand side represents the cost function of a Cauchy distribution. In this equation, μ and a are hyperparameters needed to enforce sparseness to the model; and r_i correspond to the i th element of \mathbf{r} . We then obtain

$$\mathbf{r} = [\mathbf{Z}^T \mathbf{Z} + \mu \mathbf{Q}(\mathbf{r})]^{-1} \mathbf{Z}^T \mathbf{R}, \quad (3.7)$$

Where $\mathbf{Q}(\mathbf{r})$ is a diagonal matrix of weights with elements given by

$$Q_{ii} = \frac{2a}{1 + ar_i^2}. \quad (3.8)$$

We can solve this problem iteratively by starting with an initial \mathbf{r} such that we are able to compute \mathbf{Q} , then \mathbf{r} , update \mathbf{Q} until reaching convergence as depicted in the following steps (modified from Sacchi 1997).

- (1) Start with an initial receiver function $\mathbf{r}^{(0)}$.
- (2) Select the hyperparameters, μ and a .

(3) Compute $\mathbf{Q}^{(0)}$.

(4) Iteratively solve equation (3.7) using:

$$\mathbf{r}^{(l)} = [\mathbf{Z}^T \mathbf{Z} + \mu \mathbf{Q}(\mathbf{r})^{(l-1)}]^{-1} \mathbf{Z}^T \mathbf{R},$$

where l is the iteration number.

(5) The iterative scheme is stopped when the tolerance is satisfied:

$$2 \frac{|\mathbf{J}^{(l)} - \mathbf{J}^{(l-1)}|}{|\mathbf{J}^{(l)}| + |\mathbf{J}^{(l-1)}|} \leq \text{tolerance}.$$

(6) Compute the data misfit. Select new hyperparameters if the misfit is not satisfactory.

In each iteration, the weighting matrix $\mathbf{Q}(\mathbf{r})$ is modified.

A simultaneous deconvolution of several teleseismic events can be achieved, as in Gurrola *et al.* (1995), by modifying equation (3.3):

$$\begin{pmatrix} \mathbf{R}_1 \\ \mathbf{R}_2 \\ \vdots \\ \mathbf{R}_{NR} \end{pmatrix} = \begin{pmatrix} \mathbf{Z}_1 \\ \mathbf{Z}_2 \\ \vdots \\ \mathbf{Z}_{NR} \end{pmatrix} \mathbf{r}, \quad (3.9)$$

where each \mathbf{Z}_j , and $\mathbf{R}_j [j = 1, \dots, NR (\text{number of seismic records})]$ are the same as \mathbf{Z} , and \mathbf{R} in (3) for the j th seismogram. In the same manner as in (3), we can solve for the receiver function \mathbf{r} as follows:

$$\mathbf{r} = \left[\sum_{j=1}^{NR} \mathbf{z}_j^T \mathbf{z}_j + \mu \mathbf{Q}(\mathbf{r}) \right]^{-1} \sum_{j=1}^{NR} \mathbf{z}_j^T \mathbf{R}_j. \quad (3.10)$$

Therefore, a simultaneous deconvolution is no more complex than the deconvolution of a single seismogram (Gurrola *et al.* 1995).

The selection of the hyperparameters μ and \mathbf{a} in equation (3.7) is very important; unfortunately there is no clear way to determine them *a priori* and a poor selection may lead us to an unreasonable solution. In general, we observe that μ must be small compared with \mathbf{a} to preserve fidelity with the data and, at the same time, to obtain a sparse solution. As we increase \mathbf{a} we enforce sparseness. In contrast, the solution approaches to a damped least-squares solution as \mathbf{a} tends to 0.

The hyperparameters μ and \mathbf{a} can be determined following the same procedure as in Sacchi (1997), that is, by using χ^2 statistic as a target misfit, $E[\chi^2] = N_{obs}$ (total number of observations), where the largest acceptable value is approximately $N_{obs} + 3.3\sqrt{N_{obs}}$ (Press *et al.* 1992). Using this test, we find multiple candidate pairs of parameters that produce similar misfits; however, when proper choices of μ and \mathbf{a} are introduced, the resulting receiver functions only vary in sparseness but not in the presence and timing of the main phases.

The sparse deconvolution approach requires the inversion of a non-Toeplitz matrix n times, where n is the number of iterations. The computational cost of each inversion is proportional to M^3 , where M is the dimension of the matrix. In

comparison, as shown in equation (3.5), the least-squares solution involves inverting a Toeplitz matrix that can be solved using fast methods such as Levinson recursion (Marple 1987). In this case, the number of computations needed is proportional to M^2 and, therefore, less expensive than the sparse deconvolution. However, with today's computer technology, such computational cost is insignificant. For instance, a receiver function of $N = 900$ samples and 15 iterations can be computed in 0.3 s with a 2.16 GHz Intel Core 2 Duo processor.

In the following sections, we will test the functionality and reliability of the simultaneous iterative time-domain sparse deconvolution in computing teleseismic receiver functions.

3.3 Synthetic Experiments

We performed three numerical experiments to test the effectiveness of the sparse deconvolution approach. We used the method of Randall (1989) to compute synthetic seismograms based on two simple velocity models: a two-layer velocity model of Ammon (1991), and a multilayer model of Ligorria & Ammon (1999). The resulting receiver functions are compared with two other approaches: water-level frequency-domain deconvolution (Ammon 1991) and time-domain least-squares deconvolution (Gurrola *et al.* 1995). In all cases, the resulting models ensure the same misfit (the rms difference between the estimated radial components and the observed radial components). As in Ligorria & Ammon (1999), we present the estimated receiver functions from water-level deconvolution using Gaussian width factors of 1.5 and 10 for the two-layer and

multilayer models, respectively. In the case of time-domain techniques, we performed the χ^2 test described in the previous section.

Figure 3.2 shows the computed receiver functions for the two-layer model. For this idealized case, all three methods retrieved high quality receiver functions with clear primary P_s conversions and multiples (Figure 3.3). The arrival times of the majority of the signal agree very well, though minor differences in signal amplitude are visible among the output of these three approaches. Our sparse deconvolution results appears to be more consistent with that of water-level deconvolution where little ringing, if any, is present on the receiver functions.

Consistent receiver functions can be uniformly obtained even when the input model is significantly more complex (Figure 3.4) than the previous case. This is expected since the data are broadband with good signal-to-noise levels, thus the differences between these three methods are insignificant. In Figure 3.4, the sparse deconvolution approach shows a pronounced zero-phase arrival at approximately 10 s. This is highly consistent with the results of the least-squares deconvolution; both highlight the zero-phase nature of the primary P arrival after deconvolution. In general, the sparse deconvolution slightly increases the resolution of closely spaced phases on the receiver functions. These two experiments show the functionality and reliability of the sparse deconvolution technique in determining receiver functions for relatively simple models and well-recorded data sets.

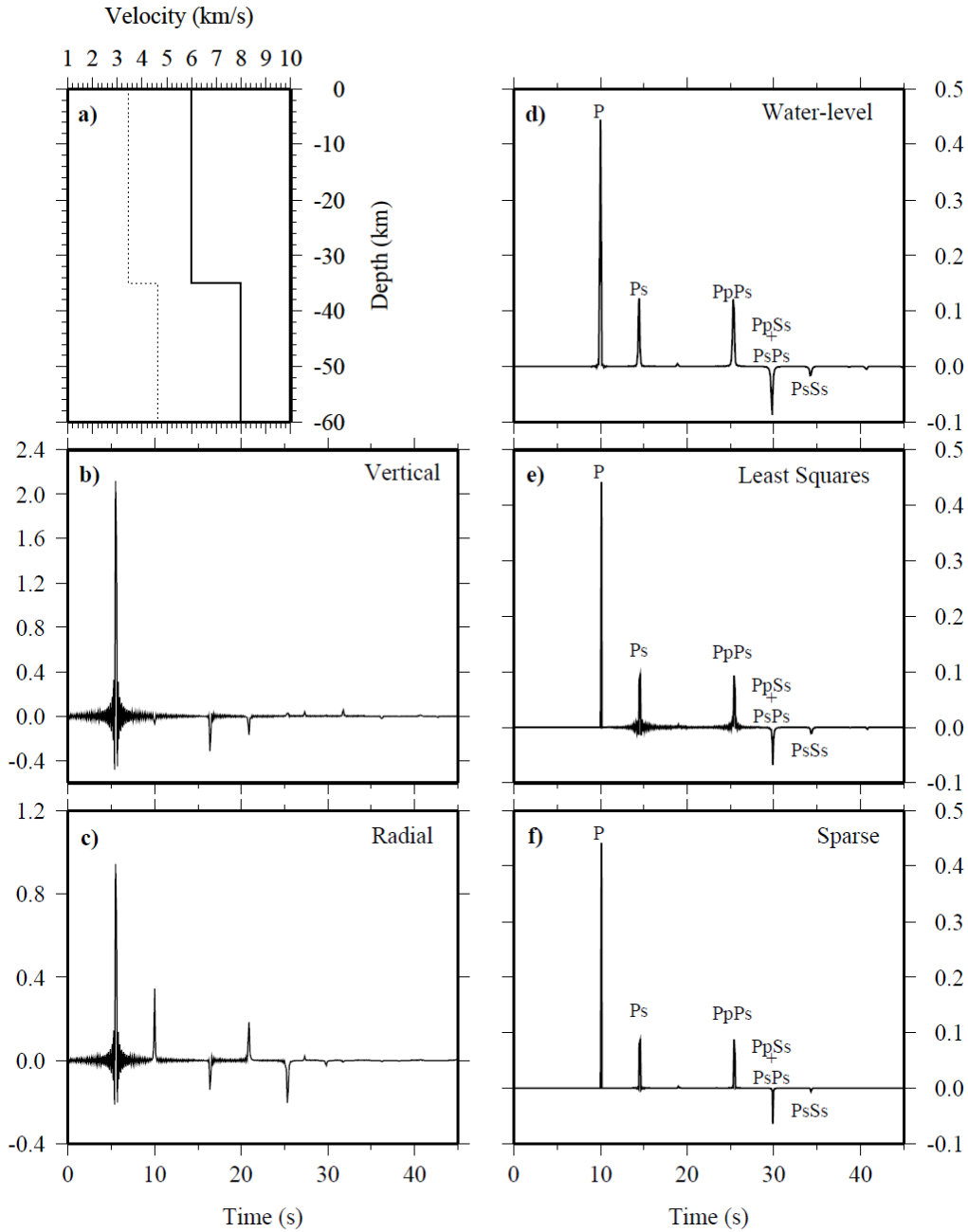


Figure 3.2: Estimated receiver functions for a simple two-layer velocity model: (1) velocity model (solid and dashed lines indicate P and S velocities, respectively); (b) vertical-component seismogram; (c) radial-component seismogram; (d) receiver function obtained after applying water-level deconvolution (Ammon 1991); (e) computed receiver function after applying the least-squares deconvolution (Gurrola *et al.* 1995) and (f) estimated receiver function using the sparse deconvolution (this study). Ps conversions and multiples are indicated.

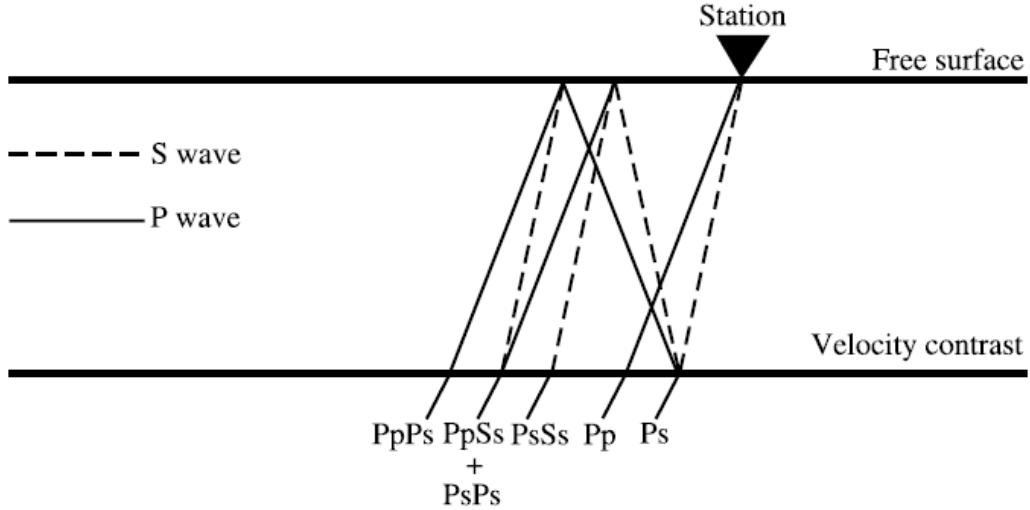


Figure 3.3: Simplified diagram showing the ray paths of the main conversions (P_s) and its multiples (P_sP_s , P_pS_s and P_pP_s). Except from the first arrival (P), upper-case letters indicate upgoing travel paths, and lower-case letters indicate downgoing travel paths (modified from Ammon 1991).

To demonstrate the distinct advantages of our sparse deconvolution approach over previous techniques, we added noise to the original vertical and radial component seismograms for the two-layer model. The computed receiver functions are presented in Figure 3.5. All the results, as in the previous tests, ensure similar misfits for a fair comparison of the models. Although not as clear as in the noise-free case (Figure 3.2), the sparse deconvolution approach is able to highlight the primary conversions and its multiples. Thus, we show the ability of our approach to compute receiver functions when dealing with less ideal data. In the following section, we use band-limited seismic data recorded in Japan to demonstrate the effectiveness of our technique to compute high-resolution receiver functions.

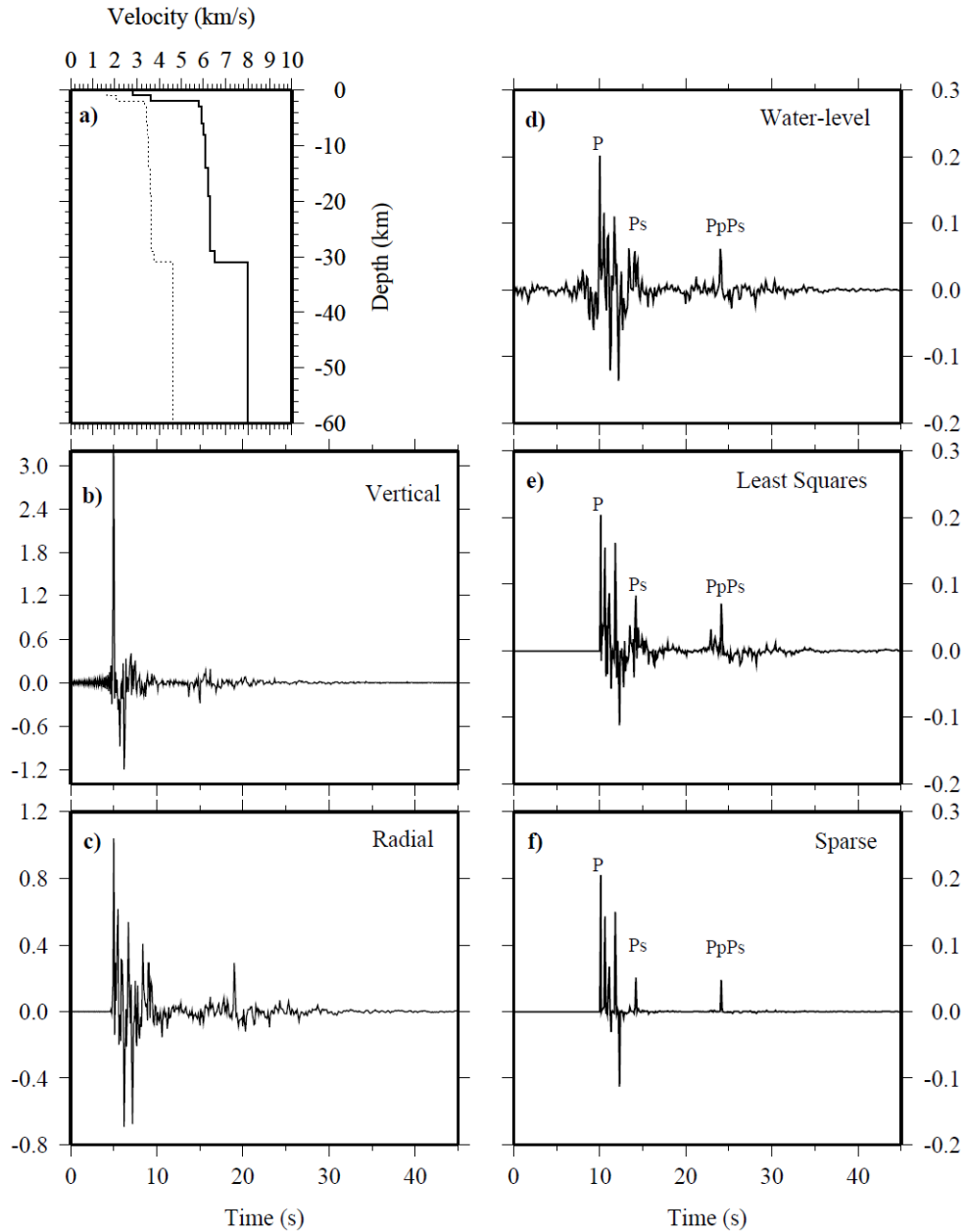


Figure 3.4: Estimated receiver functions for a multilayer velocity model: (a) velocity model (solid and dashed lines indicate P and S velocities, respectively); (b) vertical-component seismogram; (c) radial-component seismogram; (d) receiver function obtained from water-level deconvolution (Ammon 1991); (e) computed receiver function from least-squares deconvolution (Gurrola *et al.* 1995) and (f) estimated receiver function using the sparse deconvolution (this study).

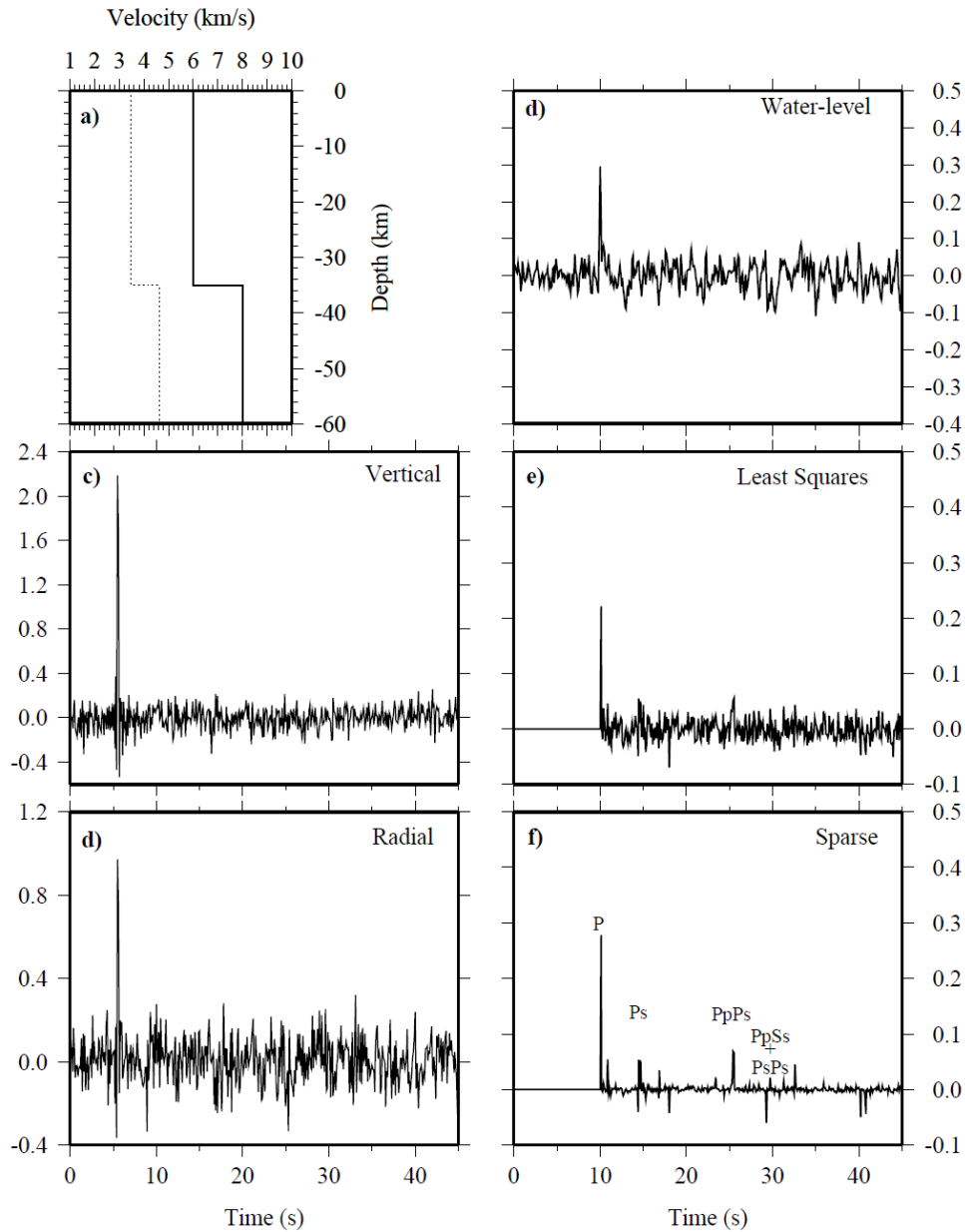


Figure 3.5: Same as in Figure 3.2 but in this case we added noise to the vertical and radial component seismograms (signal-to-noise ratio = 0.1).

3.4 Estimation of receiver functions in Southern Japan

We used seismic data recorded at station ABU (Southern Japan), from the F-net broad-band seismic array, during 2003. A total of 88 teleseismic events were

selected in the distance range between 30° and 90° with magnitudes m_b greater than 5.5 (Figure 3.6) and the event-station pairs naturally form four azimuthal bins. The small data set meets the primary objective of our pilot study, which is to evaluate the suitability of the sparse deconvolution as means to estimate high-resolution receiver functions. We used a time window of 120 s, starting 30 s before the P arrival.

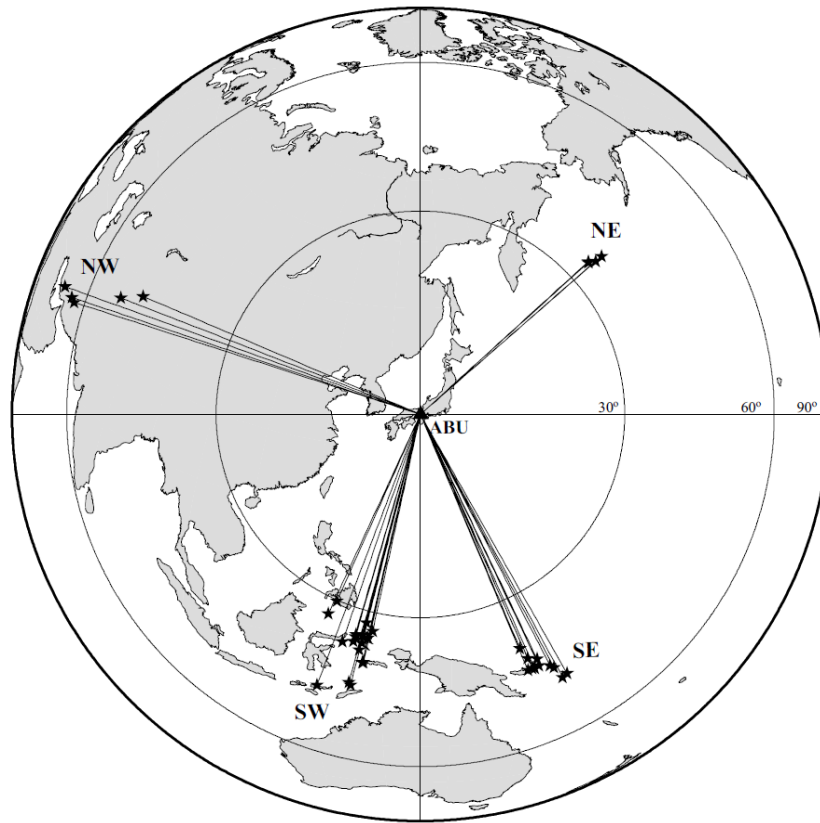


Figure 3.6: Azimuthal orthographic projection of teleseismic events recorded at station ABU, Southern Japan, during 2003. Only events from four azimuthal directions were used in this study. Equidistant lines at every 30° are shown by concentric circles. Solid lines represent ray paths.

We then performed both least-squares deconvolution (Figure 3.7a) and sparse deconvolution (Figure 3.7c) to determine the radial receiver functions for the NE azimuthal direction. We used hyperparameters ($\lambda = 10$; $\mu = 0.014$ and $a = 10000$) that produce the same misfit as shown in Figure 3.7(b) where the trade-off curves for the two approaches are displayed. In this figure, the intercepts between the trade-off curves and the dotted line indicate the hyperparameters used to compute the receiver functions.

Figure 3.7(c) demonstrates that the sparse deconvolution approach is able to provide much greater resolution and improve the identification of important phases in the receiver functions when using seismic data (band-limited data). The overall improvement results from the sparseness constraint that creates the simplest earth model possible. This will increase the frequency content since the result is composed of a superposition of broad-band spikes. Therefore, by using the sparseness constraint we are able to recover the high frequency component of the data (Sacchi 1997).

To observe the effect of the selection of hyperparameters μ and a , we computed several receiver functions using different hyperparameters while preserving the misfit for a fair comparison of the results (Figure 3.8). It is shown that as a tends to 0 the model approaches the least-squares solution (Figure 3.7a), whereas increasing a will enhance the sparseness of the solution. In general, all the solutions are similar after reaching certain a value.

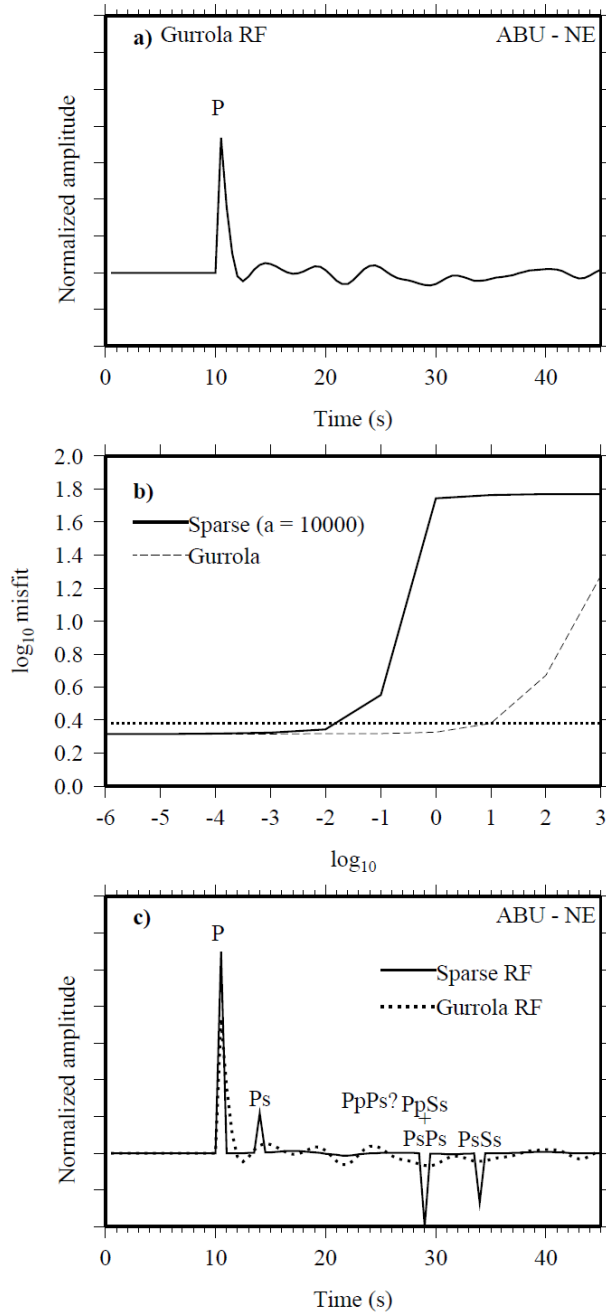


Figure 3.7: A comparison of the estimated receiver function for the NE azimuthal direction using least-squares deconvolution and the sparse deconvolution approach. (a) Receiver function obtained from least-squares deconvolution (Gurrola *et al.* 1995). (b) Trade-off curves for the least-squares approach (dashed line) and the sparse deconvolution approach (solid line). The dotted line marks the hyperparameters (intercepts with trade-off curves) used to estimate the receiver functions that produce the same misfit. (c) Receiver function determined using the sparse deconvolution (solid line); the results displayed in (a) is also shown (dashed line) for a better comparison.

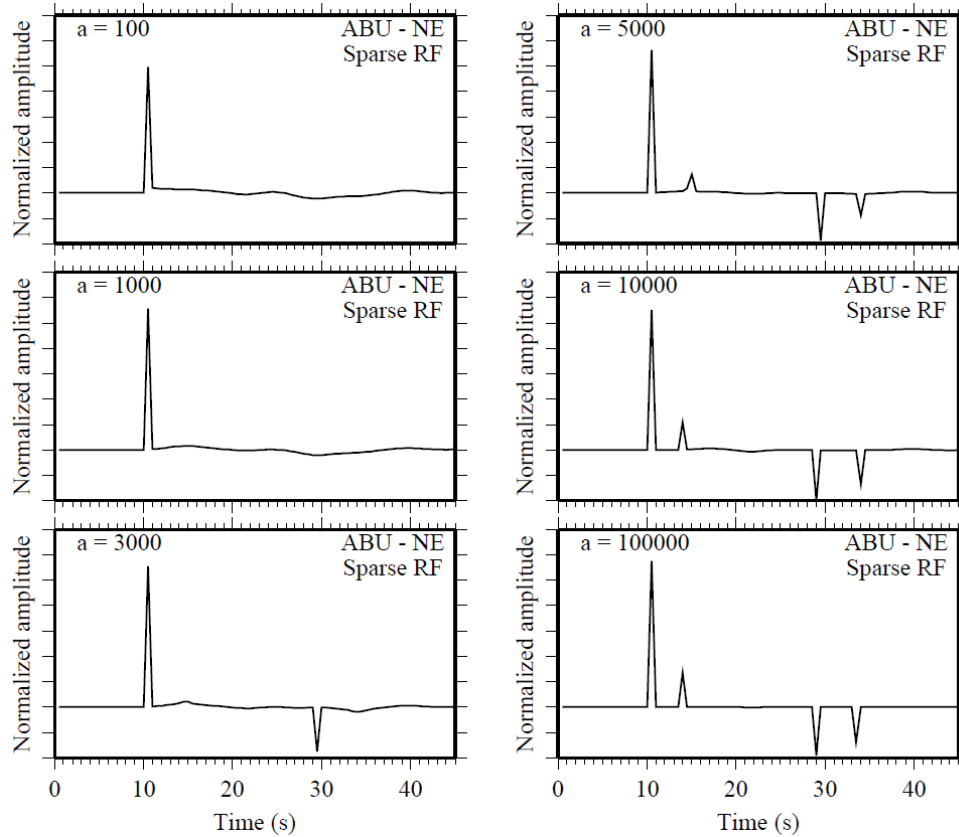


Figure 3.8: Receiver functions computed for different hyperparameters a and μ . All the resulting models ensure the same misfit. Higher a values enforce sparseness in the model. Conversely, the receiver function approaches the damped least-squares when a approaches to 0.

Figure 3.9 shows the estimated and observed radial-component seismograms after using the sparse deconvolution approach for the NE azimuthal direction. Clearly, there is a remarkable fit between the calculated seismograms and the observations, although small differences are observed, especially at the later part of the radial components.

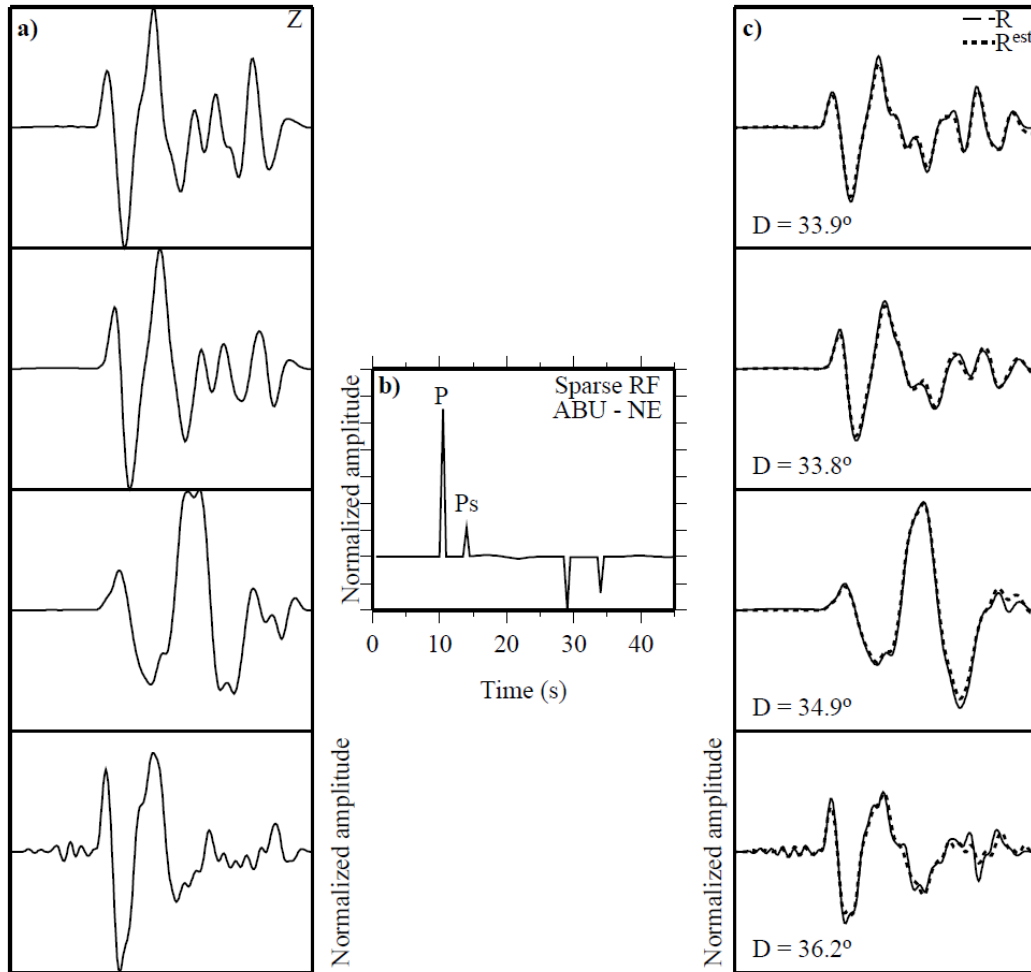


Figure 3.9: Estimated radial-component seismograms from events located in the NE azimuthal direction. (a) Vertical-component seismograms; (b) receiver functions estimated using time-domain sparse deconvolution and (c) estimated (dashed lines) and observed (solid lines) radial-component seismograms. The epicentral distances are also indicated.

The computed receiver functions for all azimuthal directions (Figure 3.10) show the same pattern with P_s conversions arriving 3.5-4.0 s after the P onset. Some multiples are also observed such as $PpPs$, $PpSs + PsPs$ and $PsSs$ at approximately 14.0, 19.0 and 25.0 s, respectively, after the P arrival. The similarity of the resulting receiver functions reflects the stability of the sparse deconvolution approach. Moreover, Li *et al.* (2000) used receiver functions to image the crustal

and upper-mantle discontinuities beneath Japan with more than 5000 teleseismic records. They found P_s conversions at around 4.0 s after the primary P arrival in areas close to station ABU which is consistent with our results.

Slight differences can be observed among the receiver functions (Figure 3.10), especially in the timing of the different phases. These differences arise due to the lack of distance and heterogeneity corrections since our main purpose is to demonstrate the functionality of this technique, rather than to provide a detailed seismic interpretation. Furthermore, the $PpPs$ multiple is notably missing on the receiver function from the NE azimuthal direction. This is because the sparse deconvolution approach tends to emphasize the most prominent features and remove small/weak phases; relatively few events (4) used in the receiver function calculations (Figure 3.6) may also contribute to the lack of this phase. In other words, a comparable resolution of the $PpPs$ with synthetic examples shown in Figure 3.2 will require data with a greater bandwidth, a denser azimuthal coverage and a high signal-to-noise ratio. It should be noted that a single receiver function using the events from all azimuthal directions can be computed, but an accurate interpretation would require proper corrections prior to the inversion procedure. Otherwise, the receiver function will be highly affected by the different traveltimes moveouts.

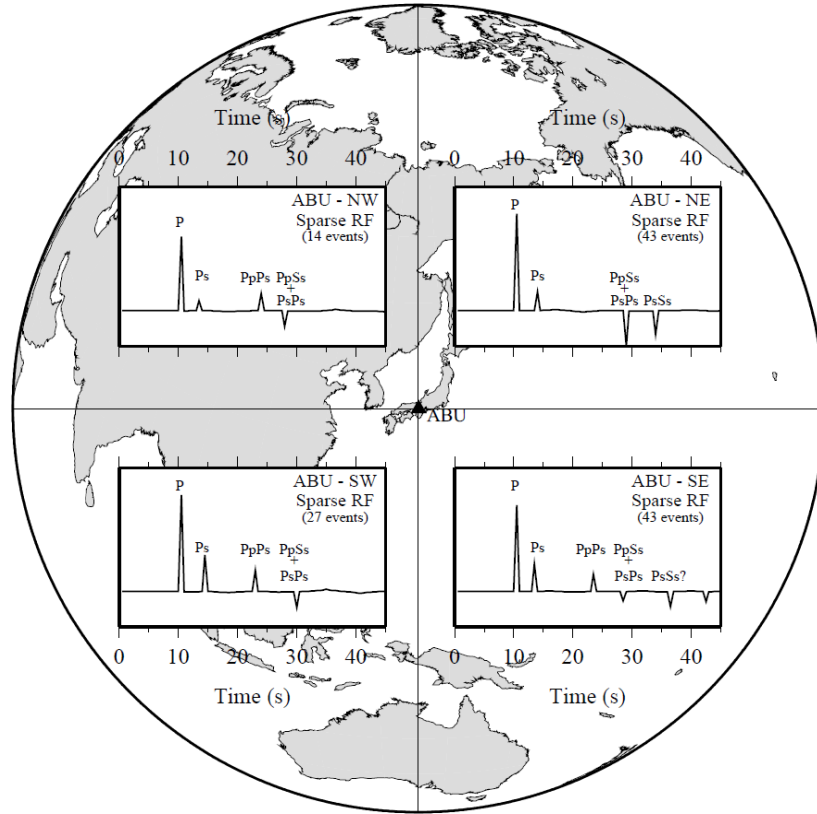


Figure 3.10: Receiver functions at station ABU (Southern Japan) estimated by the simultaneous iterative sparse deconvolution for all azimuthal directions. The number of events used to compute the receiver functions are also indicated. There are slight differences among the receiver functions, especially in the timing of the phases due to the lack of distance and heterogeneity corrections to the receiver functions.

From a broader perspective, the sparse deconvolution approach, presented here, nicely complement the ongoing global effort in providing a high-resolution image for seismic structure and discontinuity depths. Our approach can be equally effective in computing transverse receiver functions (Park & Levin 2000; Levin *et al.* 2002) that are highly sensitive to seismic anisotropy. The sparseness constraint can significantly improve the accuracy of phase identification and timing of

important phases such as *P*-to-*S* conversions. This directly translates to improved analyses of structure, interface, and anisotropy in the Earth's crust and mantle.

3.5 Conclusion

We present the sparse deconvolution as an alternative approach to existing methods such as water-level deconvolution or least-squares deconvolution for a receiver function estimation. The functionality and reliability of this new approach are examined through the applications on both synthetic and observed seismic data. The results clearly demonstrate that the simultaneous iterative time-domain sparse deconvolution is a suitable method for the determination of high-resolution teleseismic receiver functions.

3.6 References

- Abers, G.A., Hu, X. & Sykes, L.R., 1995. Source scaling of earthquakes in the Shumagin Region, Alaska: time-domain inversions of regional waveforms, *Geophys. J. Int.*, **123**, 41–58.
- Ammon, C.J., 1991. The isolation of receiver effects from teleseismic *P* waveforms, *Bull. seism. Soc. Am.*, **81**, 2504–2510.
- Ammon, C.J., Randall, G.E. & Zandt, G., 1990. On the nonuniqueness of receiver function inversions, *J. geophys. Res.*, **95**, 15 303–15 318.
- Bostock, M.G., 1996. *Ps* conversions from the upper mantle transition zone beneath the Canadian landmass, *J. geophys. Res.*, **101**, 8393–8402.
- Clayton, R.W. & Wiggins, R.A., 1976. Source shape estimation and deconvolution of teleseismic bodywaves, *Geophys. J. R. astr. Soc.*, **47**, 151–177.
- Dueker, K.G. & Sheehan, A.F., 1997. Mantle discontinuity structure from midpoint stacks of converted *P* to *S* waves across the Yellowstone hot spot track, *J. geophys. Res.*, **102**, 8313–8327.

- Escalante, C., Gu, Y.J. & Sacchi, M., 2007. Simultaneous iterative time-domain sparse deconvolution to teleseismic receiver functions, *Geophys. J. Int.*, **171**, 316-325.
- Flanagan, M.P. & Shearer, P.M., 1998. Global mapping of topography on transition zone velocity discontinuities by stacking SS precursors, *J. geophys. Res.*, **103**, 2673–2692.
- Flanagan, M.P. & Shearer, P.M., 1999. A map of topography on the 410-km discontinuity from *PP* precursors, *Geophys. Res. Lett.*, **26**, 549–552.
- Gu, Y.J. & Dziewonski, A.M., 2002. Global variability of transition zone thickness, *J. geophys. Res.*, **107**, doi:10.1029/2001JB000489.
- Gu, Y.J., Dziewonski, A.M. & Agee, C.B., 1998. Global de-correlation of the topography of transition zone discontinuities, *Earth Planet. Sci. Lett.*, **157**, 57–67.
- Gurrola, H. & Minster, J.B., 1998. Thickness estimates of the upper-mantle transition zone from bootstrapped velocity spectrum stacks of receiver functions, *Geophys. J. Int.*, **133**, 31–43.
- Gurrola, H., Baker, G.E. & Minster, J.B., 1995. simultaneous time domain deconvolution with application to the computation of receiver functions, *Geophys. J. Int.*, **120**, 537–543.
- Kind, R., Kosarev, G.L. & Petersen, N.V., 1995. Receiver functions at the stations of the German Regional Seismic Network (GRSN), *Geophys. J. Int.*, **121**, 191–202.
- Langston, C.A., 1977. The effect of planar dipping structure on source and receiver responses for constant ray parameter, *Bull. seism. Soc. Am.*, **67**, 1029–1050.
- Langston, C.A., 1979. Structure under Mount Rainer, Washington, inferred from teleseismic body waves, *J. geophys. Res.*, **84**, 4749–4762.
- Langston, C.A., 1981. Evidence for the subducting lithosphere under southern Vancouver Island and western Oregon from teleseismic *P* wave conversions, *J. geophys. Res.*, **86**, 3857–3866.
- Lawrence, J.F. & Shearer, P.M., 2006. A global study of transition zone thickness using receiver functions, *J. geophys. Res.*, **111**, doi:10.1029/2005JB003973.

- Lee, D.-K. & Grand, S., 1996. Depth of upper mantle discontinuities beneath the East Pacific Rise, *Geophys. Res. Lett.*, **23**, 3369–3372.
- Levin, V., Park, J., Brandon, M., Lees, J., Peyton, V., Gordeev, E. & Ozerov, A., 2002. Crust and upper mantle of Kamchatka from teleseismic receiver functions, *Tectonophysics*, **358**, 233–265.
- Li, X., Sobolev, S.V., Kind, R., Yuan, X. & Estabrook, Ch., 2000. A detailed receiver function image of the upper mantle discontinuities in the Japan subduction zone, *Earth Planet. Sci. Lett.*, **183**, 527–541.
- Ligorria, J.P. & Ammon, C.J., 1999. Iterative deconvolution and receiver function estimation, *Bull. seism. Soc. Am.*, **89**, 1395–1400.
- Marple, S.L., Jr., 1987. *Digital Spectral Analysis with Applications*, Prentice-Hall, New Jersey.
- Mendel, J.M., 1990. *Maximum Likelihood Deconvolution*, Springer, New York.
- Menke, W. & Levin, V., 2004. The cross-convolution method for interpreting *SKS* splitting observations, with application to one and two-layer anisotropic earth models, *Geophys. J. Int.*, **154**, 379–392.
- Oldenburg, D.W., 1981. A comprehensive solution to the linear deconvolution problem, *Geophys. J. R. astr. Soc.*, **65**, 331–357.
- Olofsson, T., 2004. Semi-sparse deconvolution robust to uncertainties in the impulse responses, *Ultrasonics*, **42**, 969–975.
- Owens, T.J. & Crosson, R.S., 1988. Shallow structure effects on broadband teleseismic *PP* waveforms, *Bull. seism. Soc. Am.*, **78**, 96–108.
- Park, J. & Levin, V., 2000. Receiver functions from multiple-taper spectral correlation estimates, *Bull. seism. Soc. Am.*, **90**, 1507–1520.
- Petersen, N., Vinnik, L.P., Kosarev, G., Kind, R., Oreshin, S. & Stammer, K., 1993. Sharpness of the mantle discontinuities, *Geophys. Res. Lett.*, **20**, 859–862.
- Pham, T. & de Figueiredo, R., 1989. Maximum likelihood estimation of a class of non-Gaussian densities with application to *l p* deconvolution, *IEEE Trans. Signal Proc.*, **37**, 73–82.
- Press, W., Teukolsky, S., Vetterling, W. & Flannery, B., 1992. *Numerical Recipes*, Cambridge University Press, Cambridge.

- Randall, G.E., 1989. Efficient calculation of differential seismograms for lithospheric receiver functions, *Geophys. J. Int.*, **99**, 469–481.
- Ringwood, A.E. & Irifune, T., 1988. Nature of the 650-km seismic discontinuity - implications for mantle dynamics and differentiation, *Nature*, **331**, 131–136.
- Sacchi, M.D., 1997. Reweighting strategies in seismic deconvolution, *Geophys. J. Int.*, **129**, 651–656.
- Shearer, P.M., 2000. Upper mantle seismic discontinuity, in *Earth's Deep Interior: Mineral Physics and Tomography from the Atomic to the Global Scale*, AGU Geophysical Monograph, Vol. 117, 115–131. *Nature*, **355**, 791–796.
- Shearer, P.M. & Masters, G., 1992. Global mapping of topography on the 660-km discontinuity, *Nature*, **355**, 791–796.
- Sheehan, A.F., Abers, G.A., Jones, C.H. & Lernerlam, A.L., 1995. Crustal thickness variations across the Colorado Rocky-Mountain from teleseismic receiver functions, *J. geophys. Res.*, **100**, 20 391–20 404.
- Shen, Y., Solomon, S.C., Bjarnason, I.T. & Purdy, G.M., 1996. Hot mantle transition zone beneath Iceland and the adjacent Mid-Atlantic Ridge inferred from *P*-to-*S* conversions and the 410- and 660-km discontinuities, *Geophys. Res. Lett.*, **23**, 3527–3530.
- Shen, Y., Sheehan, A.F., Dueker, K.G., de Groot-Hedlin, C. & Gilbert, H., 1998. Mantle discontinuity structure beneath the southern East Pacific Rise from *P*-to-*S* converted phases, *Science*, **280**, 1232–1235.
- Stixrude, L., 1997. Structure and sharpness of phase transitions and mantle discontinuities, *J. geophys. Res.*, **102**, 14 835–14 852.
- Vinnik, L.P., Kosarev, G. & Petersen, N., 1996. Mantle transition zone beneath Eurasia, *Geophys. Res. Lett.*, **23**, 1485–1488.
- Youzwishen, C.F., 2001. Non-linear sparse and blocky constraints for seismic inverse problems, *MSc Dissertation*, University of Alberta, 167 pp.
- Yuan, X., Ni, J., Kind, R., Sandvol, E. & Mechie, J., 1997. Lithospheric and upper mantle structure of southern Tibet from a seismological passive source experiment, *J. geophys. Res.*, **102**, 27 491–27 500.

Zhu, L., 2004. Lateral variation of the Tibetan lithospheric structure inferred from teleseismic waveforms, in *Advancements in Seismology and Physics of the Earth Interior in China*, Seismology Press, Beijing.

Zhu, L. & Kanamori, H., 2000. Moho depth variation in Southern California from teleseismic receiver functions, *J. Geophys. Res.*, **105**, 2969–2980.

CHAPTER 4

HIGH-RESOLUTION IMAGING OF THE MANTLE TRANSITION ZONE BENEATH JAPAN FROM SPARSE RECEIVER FUNCTIONS

4.1 Introduction

The study of the mantle transition zone beneath Japan is important for the determination of tectonic regimes, the thermal and geological evolution of the Japanese islands, and the understanding of the regional convection style and forces. The mantle transition zone is a region bound by two major velocity variations within the Earth's upper mantle at 410 and 660 km depth, which is the boundary to the lower mantle. These sharp velocity variations are known as the 410- and 660-km discontinuities, respectively. These discontinuities exhibit global and local undulations due to both thermal anomalies in the mantle and the Clapeyron slope associated with mineral phase transformations; and play an important role in mantle dynamics and mineral physics of the mantle, in particular the 660-km discontinuity, either hindering or allowing whole mantle convection (Ringwood, 1994).

The mantle transition discontinuities are believed to represent olivine phase changes, where increases in density produce abrupt velocity increases with depth (Helffrich, 2000; Shearer, 2000). Olivine, $(\text{Mg,Fe})_2\text{SiO}_4$, represents 40 to 60% of the mantle and undergoes phase transformations with depth due to temperature

and pressure variations (Figure 1.1). The 410-km discontinuity is commonly interpreted as a phase transformation from α -olivine to β -olivine (wadsleyite), with a positive Clapeyron slope (Katsura and Ito, 1989); while the 660-km discontinuity represents a phase change from ringwoodite (γ -olivine), which has a spinel structure, to magnesium perovskite, $(\text{Mg,Fe})\text{SiO}_3$, plus magnesiowüstite, $(\text{Mg,Fe})\text{O}$ (Ringwood, 1991) with a negative Clapeyron slope (Ito and Takahashi, 1989; Bina and Helffrich, 1994). In recent years, many studies have reported a mid-transition zone discontinuity at 520 km (Shearer, 1990, 1991, 1996; Ryberg et al., 1997, Deuss and Woodhouse, 2001); however, it is still controversial whether this discontinuity exhibits a global or only a regional presence, as it is not observed in many seismological studies (Cummins et al., 1992; Bock, 1994). It appears that majorite garnet plays an important role in the 520-km discontinuity as the olivine transition may occur over too wide a depth range to be observed in the seismic data (Shearer, 1990).

At subduction zones, such as Japan, understanding the interaction between subducting slabs and the mantle transition zone discontinuities may help to solve one of the most intriguing questions of whether convection involves a one-layer (whole mantle convection), or two-layer (upper and lower mantle, respectively) convection regime. This would provide more information about the presence of possible chemical heterogeneities carried down by the subduction process to these depths (Stixrude & Lithgow-Bertelloni, 2012). Several global tomographic images (Fukao et al., 1992, 2001; Zhou, 1992; van der Hilst et al., 1997, 2011,

etc.) show evidence of slab penetration into the lower mantle, changing a long held view of the discontinuity as a boundary that separates geochemical reservoirs and isolates the lower mantle from plate tectonic mixing. Nonetheless, several other tomographic studies show evidence of slab stagnation on the top of the 660-km discontinuity (Fukao et al., 2009, van der Hilst, 2011) causing, in some cases, a deflection of the 660-km discontinuity. These discrepancies could be due to the limitation in resolution of the tomographic images laterally and vertically; mainly resulting from the uneven distribution of seismic stations and earthquakes to produce a dense coverage of the study areas. Therefore, it is necessary to use other high-resolution techniques to image these discontinuities at a regional and/or local scales, such as receiver functions.

Japan is an ideal location to study this problem not only because of the large number of seismic stations covering the whole Japanese island but also because of the active seismicity in this region that allows tracking the subducting Pacific slab from the Japan trench to depths down to 700 km. Recent global and regional tomographic observations (Fukao et al., 2009; van der Hilst et al., 2011) show that subducted Pacific slab is deflected sub-horizontally around the 660-km discontinuity for over 1000 km beneath north-eastern China in good agreement with SS precursor data (Shearer et al., 1992, 1998, 1999). The magnitude of this deflection varies from 20 to up to 40 km. High-resolution studies at local scale suggest that the 660 km discontinuity is depressed by up to 80 km due to the stagnation of the subducted Pacific slab (Castle and Creager, 1997; Li and Yuan,

2000, Tonegawa et al., 2005; Niu et al., 2005). The 410-km discontinuity also shows an upward undulation where the subducting Pacific slab reaches this discontinuity with amplitudes ranging from 10 to 40 km (Vidale and Benz, 1992; Tonegawa et al., 2005; Niu et al., 2005).

In an attempt to improve the current mantle transition zone picture beneath Japan, in this study, sparse receiver functions were used to reveal the detailed structure and topography of these discontinuities and their interaction with the subducting Pacific plate. The large number of high-quality waveforms recorded by the FNET seismograph network, a high-density broadband seismic network covering the whole Japanese island, makes it possible to achieve a significant resolution enhancement of the transition zone imaging in comparison with previous receiver function studies in this region detecting small-scale topographic undulations of the 410-km and 660-km discontinuities.

4.2 Seismological data, Data Selection, and RF Processing

4.2.1 F-NET Broadband Seismograph Network

The database was constructed from seismic waveforms recorded at about 82 broadband seismic stations from the F-NET broadband seismograph network (Figure 4.1) during the years 2003-2006. The F-NET network is a network of approximately 90 seismic stations administrated by the Japanese National Research Institute for Earth Science and Disaster Prevention (NIED). Initially,

after the 1996 Kobe Earthquake, this network started under the name of FREESIA (Fundamental Research on Earthquakes and Earth's Interior Anomaly); however, in April 2003, the FREESIA project and several stations of about 20 universities merged into the F-NET network in order to cover the whole Japanese islands.

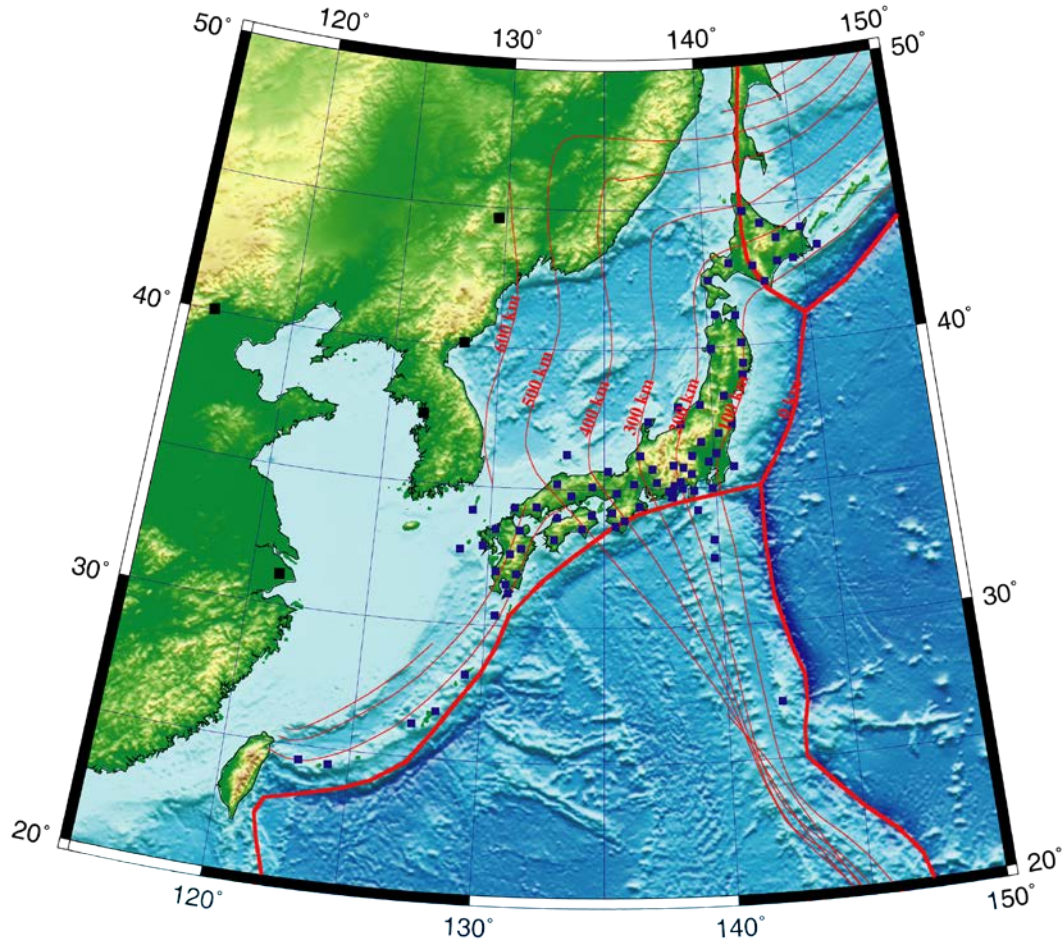


Figure 4.1: F-NET broadband seismograph network. Blue squares indicate F-NET stations. Thick and thin red lines denote the plate boundaries and contour depths of the top surface of the Pacific slab determined by distribution of deep and intermediate-deep earthquakes, respectively.

Based on the experience to construct FREESIA, the F-NET network was required to have an average spacing of 60 km providing a dense and uniform network. The

seismometers are installed in 30 to 50-meter long vaults due to the sensitivity to temperature variations. Initially, STS-1 sensors were used at 22 stations; however since the manufacturing of these sensors was stopped, STS-2 seismometers were installed in the remaining stations (further details can be found in Appendix 1).

The data acquisition, monitoring, processing, and archiving are controlled by the database management system created by NIED. It automatically carries out a series of data processing steps, including determination of moment tensor solutions which are later corrected by operators to improve the quality of the results (Okada *et al.* 2004). Waveform data obtained from the F-NET stations are archived and provided to the researchers and general public through the internet (<http://www.fnet.bosai.go.jp>). Users can retrieve raw data of continuous waveforms of arbitrary stations and can also browse moment tensor solutions.

4.2.2 Data Selection

The receiver functions (RF) were constructed using waveforms for over 250 teleseismic events with body wave magnitudes (m_b) larger than 5.5 occurring during the period of 2003-2006. The epicentral distribution of the teleseismic events used in this study is shown in Figure 4.2. Only teleseismic events with angular distances ranging from 30 to 90 were selected, with back azimuths in almost of directions. The dataset consisted of about 20,000 waveforms, of which 9,534 waveforms with good signal to noise ratios were selected for computing the simultaneous sparse RFs with a source time window of 150 s (30 s before and 120 s after the P wave arrival).

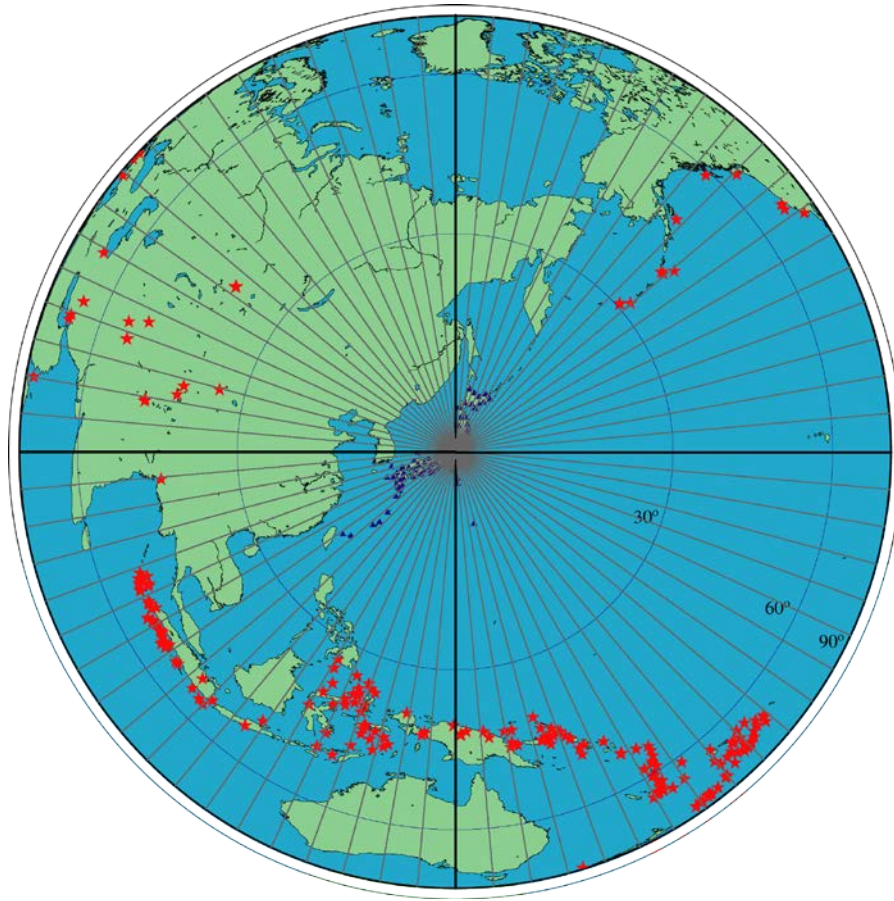


Figure 4.2: Distribution of the teleseismic events used in this work. Distances (in degrees) are with respect to the centre of the study area. Red stars and blue triangles indicate the location of teleseismic events and F-NET seismic stations, respectively. Black lines indicate 5° azimuthal bins used for computing the sparse receiver functions for station ABU, southern Japan.

The conversion points at the 410- and 660-km depths are displayed in Figure 4.3 and 4.4, respectively. The dense coverage of the study region, in conjunction with the high-quality data, guarantees enough resolution to provide a detailed image of the upper mantle seismic structure beneath Japan.

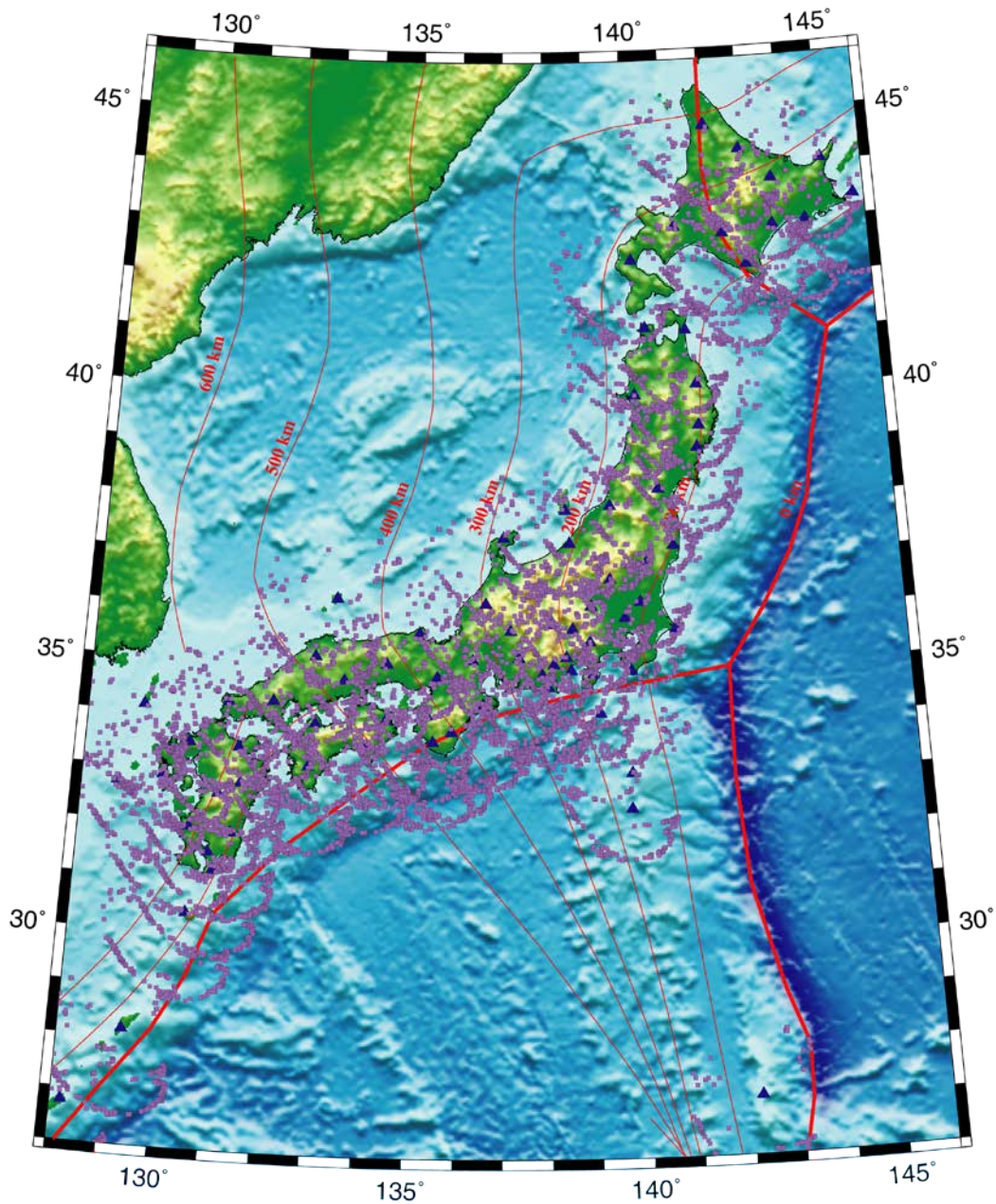


Figure 4.3: Piercing points of Ps converted phases at a depth of 410 km indicated by purple squares. Blue triangles indicate F-NET station locations. Thick and thin red lines indicate plate boundaries and contour depths corresponding to the top surface of the subducting slabs obtained from the distribution of deep and intermediate-deep earthquakes, respectively.

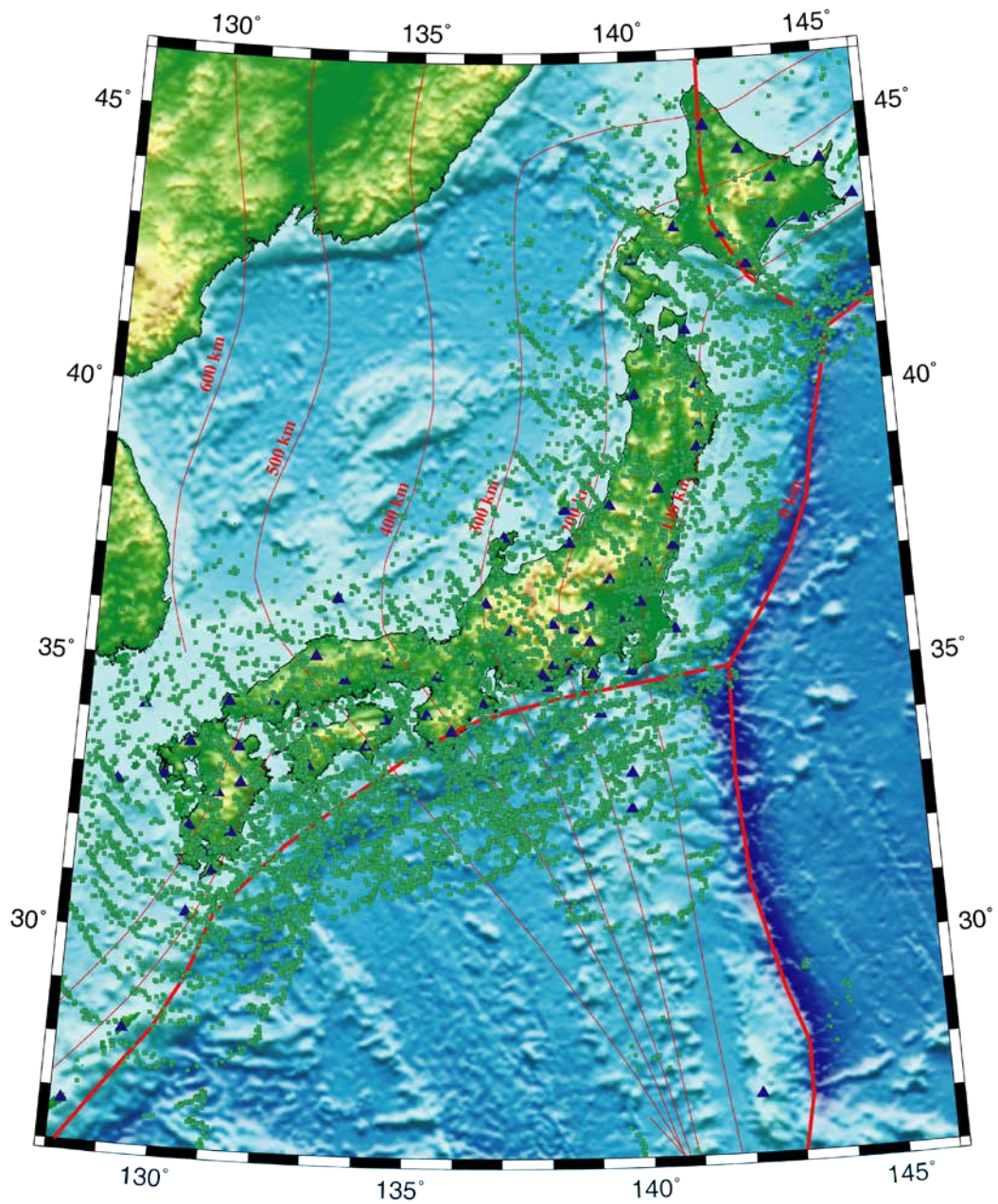


Figure 4.4: Same as Figure 4.3 but at 660 km. Green squares and blue triangles indicate piercing points of Ps converted phases and F-NET station locations.

4.2.3 *P-Wave Travel Time Picking*

As described in the previous section, the selected data use a source time window of 150 s relative to the primary *P* arrival time. Since many of the arrival times of *P* waves corresponding to a seismic event were recorded simultaneously at more than one station, and to preserve the coherence of travel time picking, a multichannel phase cross-correlation (MPCC) technique (Schimmel 1999, 2003; Escalante 2001) was adapted for the determination of relative arrival times. This is fundamental since many waveforms, corresponding to different seismic events, are simultaneously used to estimate each sparse RF, as discussed in Chapter 3.

The MPCC technique determines the similarity of the greatest number of coherent samples rather than the largest sum of cross products. Therefore, it is not biased by the large amplitude portions in the correlation window. The data were inspected event by event and the correlation windows were selected by hand to include the first swing of the signal. Initially, the data are aligned with respect to their theoretical *P* wave arrival time estimated for a global reference model PREM (Dziewonski & Anderson 1981). Once the MPCC is applied the data is aligned with respect to their relative arrival times (Figure 4.5) and the waveforms are sliced 30 s before and 120 s after these times.

The MPCC results were manually checked to avoid cycle skipping and phase misinterpretation. Poor signals were correlated using different settings and discarded if the results were not satisfactory and consistent.

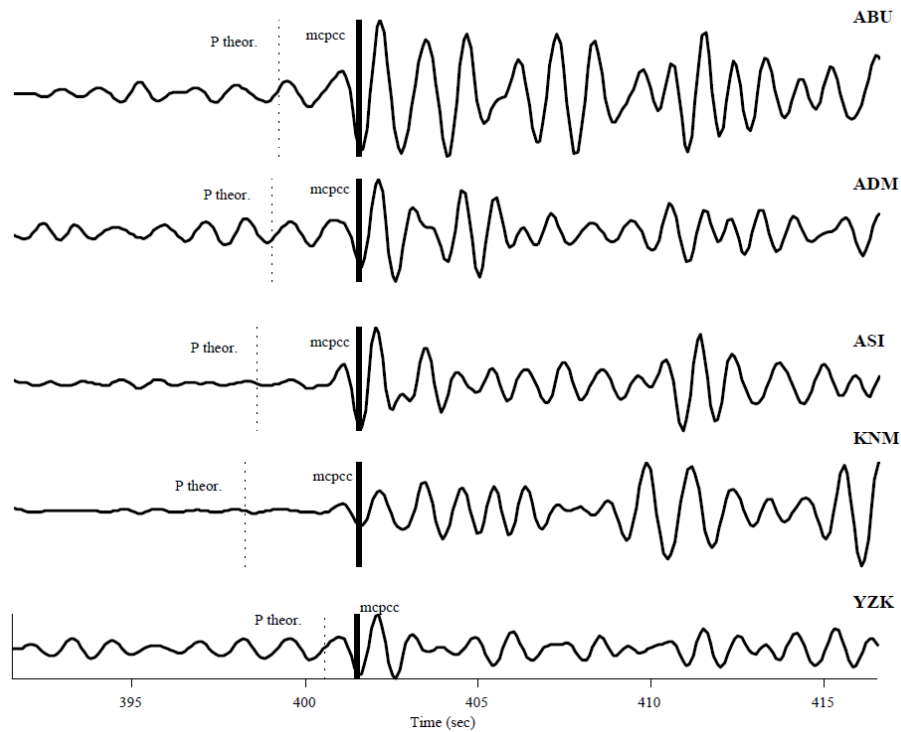


Figure 4.5: Vertical component broadband recordings for an event at the Aleutian Islands. The traces are aligned with respect to their relative arrival times. Note the resulting signal coherence.

4.2.4 Receiver Function Processing

Following the methodology described in Escalante et al. (2007) and Chapter 3, the radial RFs were computed using the sparse deconvolution approach. All the seismic data, for each station, were separated in 5° azimuthal bins (Figure 4.1) and the sparse receiver functions were computed for each bin, with available data. Figure 4.6 shows the results for station ABU. In this case, the sparse receiver functions show the same pattern with clear P_s conversions arriving at approximately 46 and 70 seconds after the primary P arrival possibly associated to the $P410s$ and $P660s$ conversions respectively. These results are in good

agreement with previous studies in the same area (Li *et al.*, 2000; Niu *et al.*, 2005).

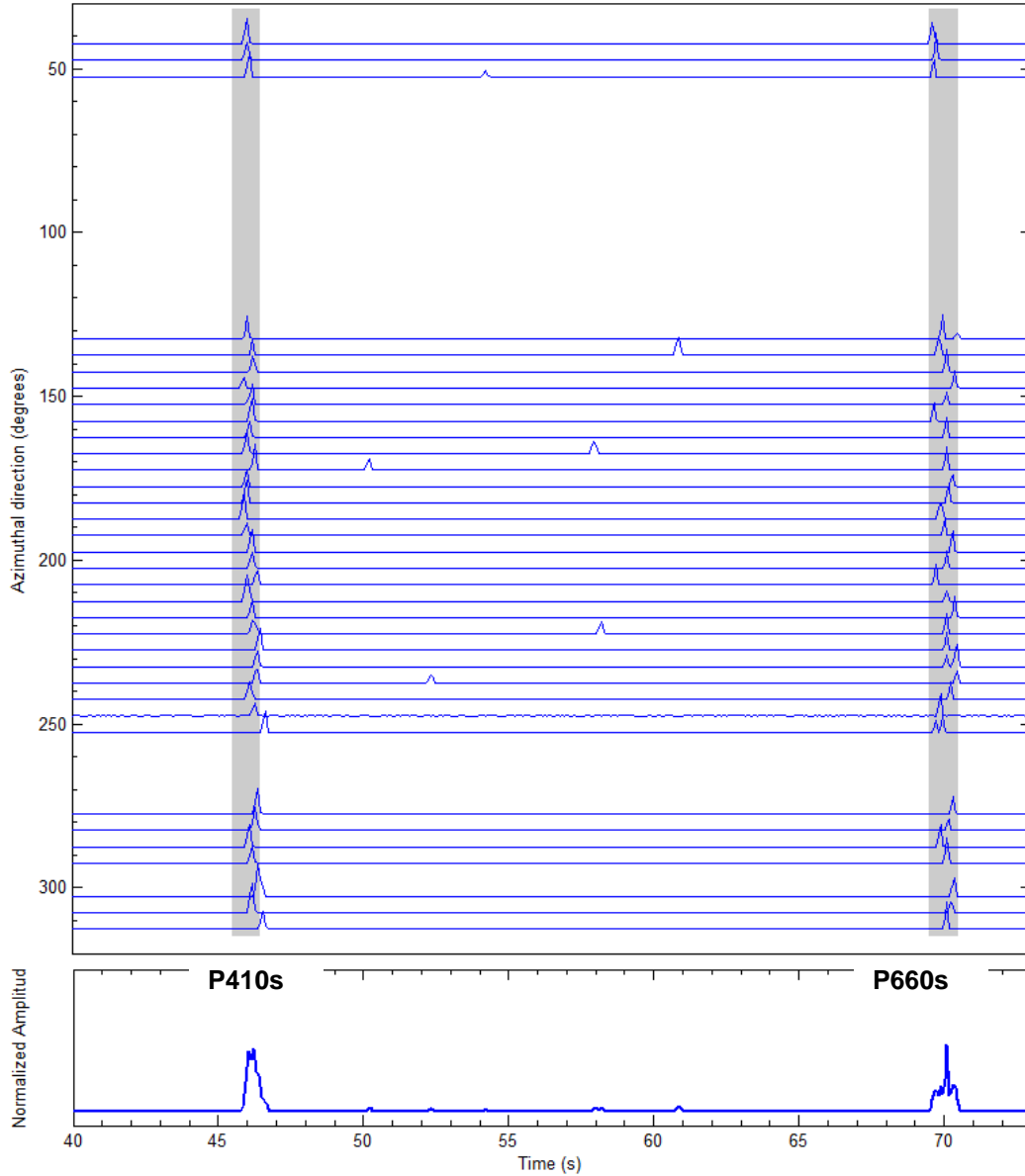


Figure 4.6: Estimated sparse receiver functions for station ABU, southern Japan. Each receiver function corresponds to an individual azimuthal bin. Identification of P_s converted phases at the 410 and 660-km discontinuity is indicated. Lower panel shows the stacked receiver function.

To image the topography of the 410- and 660-km discontinuities, a depth conversion of the sparse receiver functions is required. This conversion was achieved by employing the ray-path of the *Ps* converted phases computed based on an average 1D velocity model derived from a high-resolution 3D tomographic velocity model for Japan (Nakamura *et al.*, 2000) and projecting the resulting depth to the *Ps* converted points (Figures 4.3 and 4.4 for the 410- and 660-km discontinuities, respectively). Finally, the average depths for the 410- and 660-km discontinuities were estimated and plotted in $0.5^\circ \times 0.5^\circ$ bins. The results are shown in Figures 4.7 and 4.8 for the 410- and 660-km discontinuity respectively.

4.3 Results

Figures 4.7 and 4.8 show measured depths of the 410- and 660-km discontinuities, respectively. The results indicate no major topographic variations of the 410-km discontinuity with an estimated average depth of 412 km. The only distinct feature observed is a locally elevated 410-km discontinuity along the 300-400 km contour of the Wadati-Benioff zone with a topographic relief of up to 10 km. This anomalous region seems to correlate well with the penetration of the subducting Pacific plate into the 410-km discontinuity and is in good agreement with previous studies (Li *et al.*, 2000; Tonegawa *et al.*, 2005; 2008) in this area.

In case of the 660-km discontinuity (Figure 4.8), a significant westward depression is observed with a very broad topographic low with amplitudes of up to ~30 km. This topographic depression covers almost all Southwestern Japan and potentially extends further to the west beneath the Korean Peninsula (the average

depth of the 660-km discontinuity is estimated at 668 km). These observations may indicate that this deflection is the result of a flat lying slab on the top of the 660-km discontinuity consistent with some of the global tomographic images which show a sub-horizontal high velocity anomaly at these depths in the same study region (Fukao et al., 2001).

Figure 4.9 shows the mantle transition zone thickness beneath Japan. A thickening of the transition zone (~290 km) is clearly observed within the region of the slab where the Pacific plate interacts with the 410- and 660-km discontinuity. This is expected as the presence of the cooler material associated to the subducting slab decreases the temperature of the transition zone; and the overlying and underlying mantle.

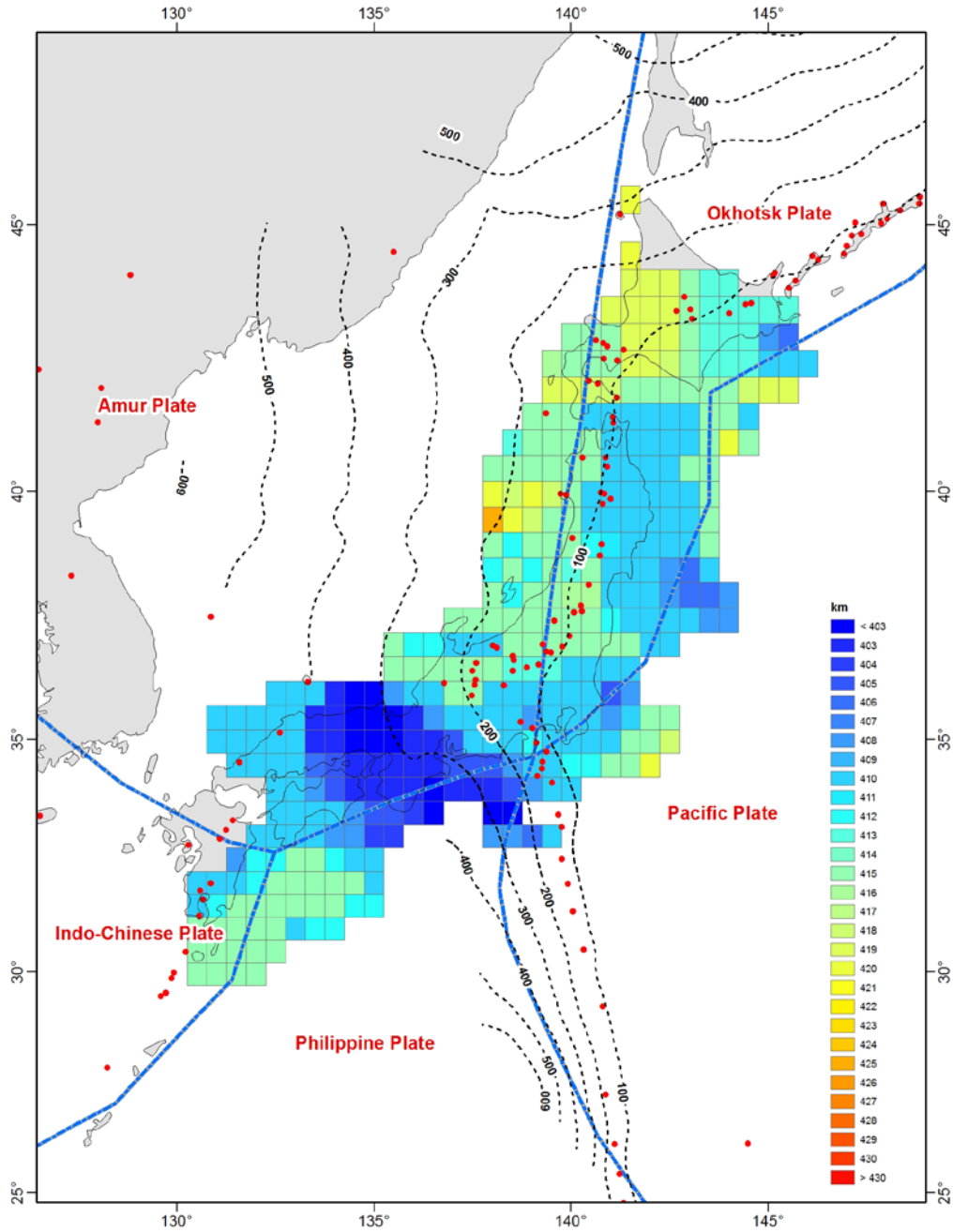


Figure 4.7: Depth distribution of the 410-km discontinuity. Red triangles indicate F-NET station locations. Black dotted lines (contour depths) correspond to the top surface of the subducting slabs obtained from the distribution of deep and intermediate-deep earthquakes.

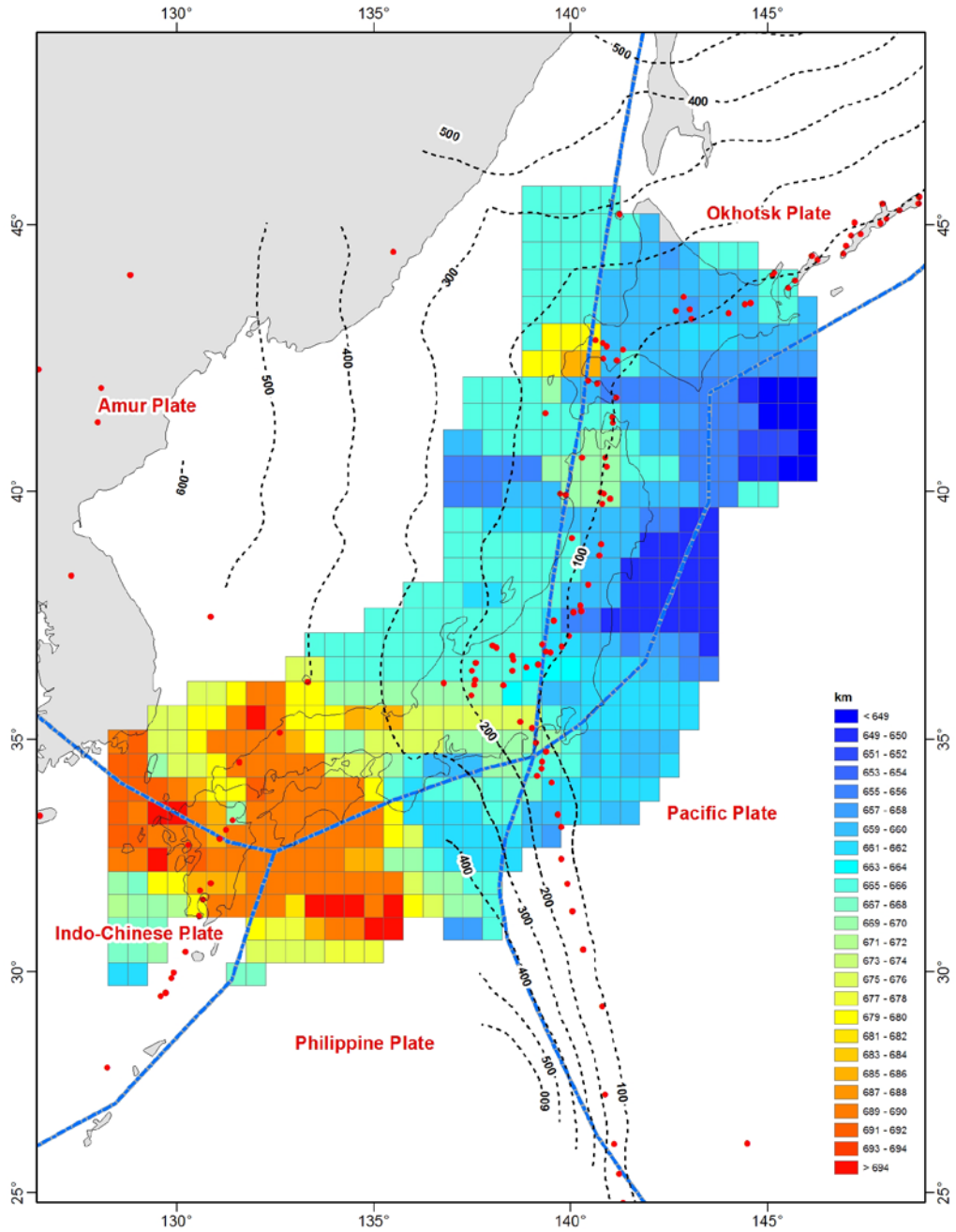


Figure 4.8: Same as Figure 4.6 but for the 660-km discontinuity.

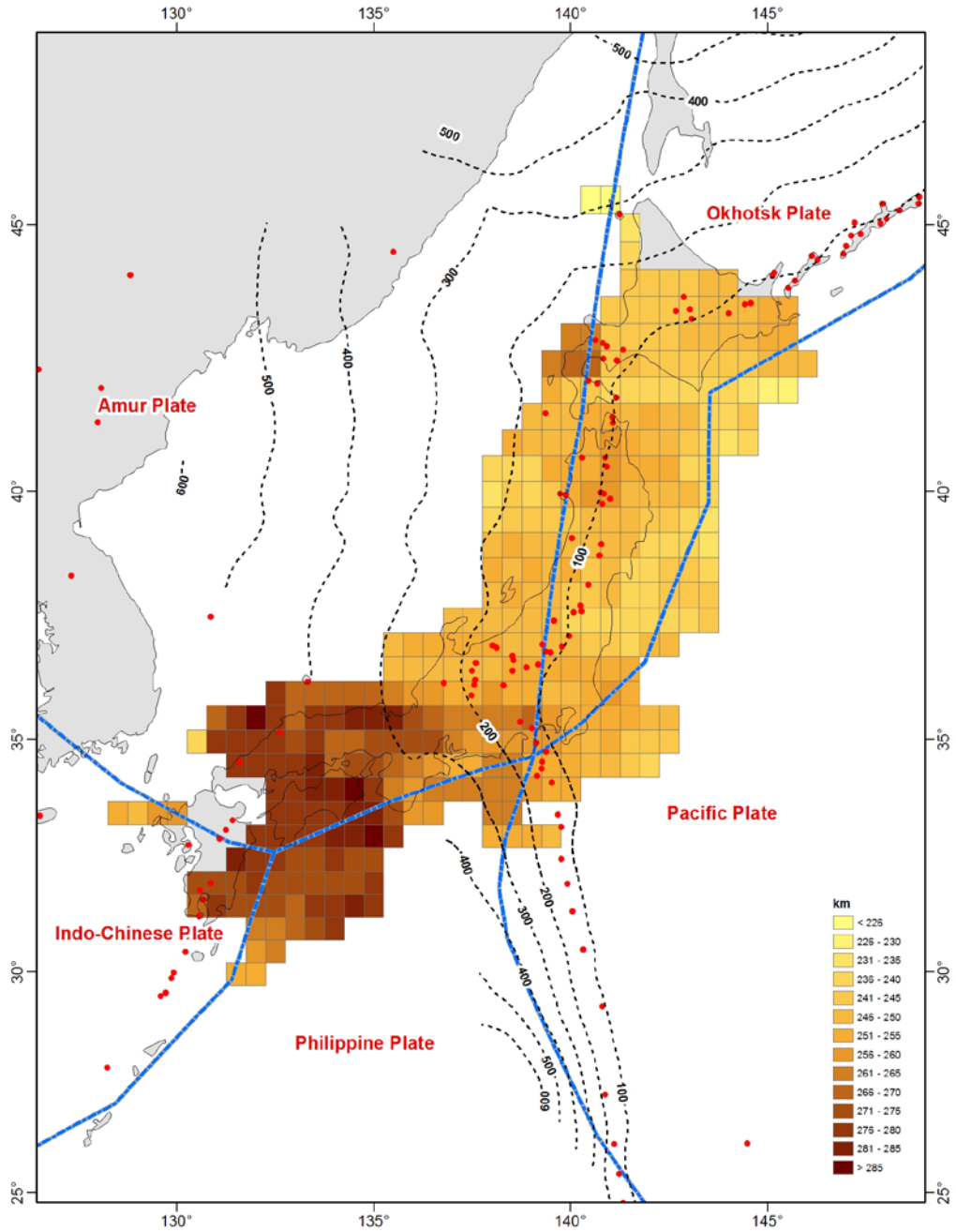


Figure 4.9: Thickness of the mantle transition zone. Symbols and lines are the same as in Figure 4.6.

4.4 Discussions

The arrival times of the Ps converted phases at the 410- and 660-km discontinuities are often used to probe mantle temperatures, especially to search for the effect of mantle plumes and subducting plates (Shen et al., 1996, 1998, 2002; Foulger et al., 2000). The 410-km discontinuity is due to the exothermic olivine to wadsleyite phase change, which has a Clapeyron slope of approximately 2.9 MPa K^{-1} , and the 660-km discontinuity is due to the endothermic ringwoodite to magnesiowustite and perovskite phase change, with a Clapeyron slope of $\sim 2.1 \text{ MPa K}^{-1}$ (Bina & Helfrich, 1994). If the mantle temperature increases, the 410-km discontinuity is expected to move deeper and the 660-km discontinuity shallower, therefore reducing the thickness of the mantle transition zone. Conversely, if the temperature is lower than the mantle average, the transition zone is expected to increase in thickness, which is the case in regions of subducting slabs such as in Japan. It is also known that a region of metastability may exist inside the cold slab where the temperature remains sufficiently low to delay the phase transformation. If the subducting slab includes such a metastable zone below the 410-km discontinuity, the olivine to wadsleyite phase boundary will be significantly depressed within the slab. However, this is difficult to image despite the high resolution of the sparse receiver function analysis.

Several tomographic studies indicate that the subducted Pacific plate does not penetrate into the lower mantle and stays stagnant at the base of the transition beneath the Japan subduction zone (Figure 4.10), creating a deflection of the 660-

km discontinuity consistent with the results obtained in this study. This deflection could be produced by a shallow dip angle associated with a rapid retrograde trench migration resulting in a flat lying slab when encountering resistance due to the negative Clapeyron slope of the post-spinel phase transition and the rapid increase in viscosity at the 660-km discontinuity (Christensen, 1996; Zhong & Gurnis, 1997; Fukao et al., 2009). Alternatively, if the subducting slab suffers significant deformation, due to a strong resistance from the lower mantle or a buoyant subducting slab, the whole transition zone can be filled up with the slab. The presence of chemical heterogeneities in the mantle can also facilitate the accumulation of crustal material at the base of transition zone or deeper at the core-mantle boundary (Stixrude & Lighthow-Bertelloni, 2012). These heterogeneities are produced at the near the surface and are continuously dragged down into the mantle via subduction. If the subducted oceanic crust is denser than depleted residue at these depths, the density contrast at the base of the transition zone may serve to accumulate heterogeneity which could be detectable by its seismic signature (Stixrude & Lighthow-Bertelloni, 2012).

Our results show a broad, large deflection of the 660-km discontinuity which is interpreted as the effect of stagnation of the subducted Pacific plate. If the subducted slab were to penetrate deeper in the lower mantle, the seismic signature associated to the 660-km discontinuity would return to its average position at around 650-660 km depth. Instead, this deflection is observed even further to the west beneath Korea, consistent with recent high-resolution tomographic studies that show that the subducted Pacific plate simply does not penetrate deep into the

lower mantle and remains flat in the transition zone (Fukao et al. 2001, 2009; Tonegawa et al., 2005, 2008). However, it is worth mentioning that since the seismic network is only in Japan, it is difficult to constrain in greater details the western part of the 660-km discontinuity. Additional data recorded by seismic stations from the north-eastern China and Korea (similar to Wang & Niu, 2011; and Gao *et al.*, 2010) would be needed to better map the transition zone discontinuities beneath these regions and; therefore, have a complete picture of the subduction processes at these depths.

4.5 Conclusions

In this study, the simultaneous sparse deconvolution analysis for computing teleseismic receiver functions (sparse receiver functions) was applied to obtain a high resolution image of the topography of the mantle transition zone discontinuities beneath Japan. The results show a locally elevated 410-km discontinuity with a topographic relief of up to 10 km in a region coincident with the subducting Pacific plate; conversely, the 660-km discontinuity shows a significant large depression of up to ~30 km well in agreement with the stagnation of the Pacific plate at these depths. These results are consistent with previous receiver function studies and with global tomographic images of a flat lying slab in this region. It is still debatable whether parts of the deflected slab is sinking into the lower mantle or not; since this is not really clear with our observations. But it appears that the 660-km discontinuity deflection extends further to the west into the Korean Peninsula. However, larger station coverage, including stations from Korea and north-eastern China, is necessary to better image the whole

subducting slab in the north-western Pacific in order to improve our understanding of the deep subduction processes and their geodynamical implications. This study also demonstrates the effectiveness and applicability of the sparse receiver functions as an alternative tool for high-resolution imaging of seismic discontinuities.

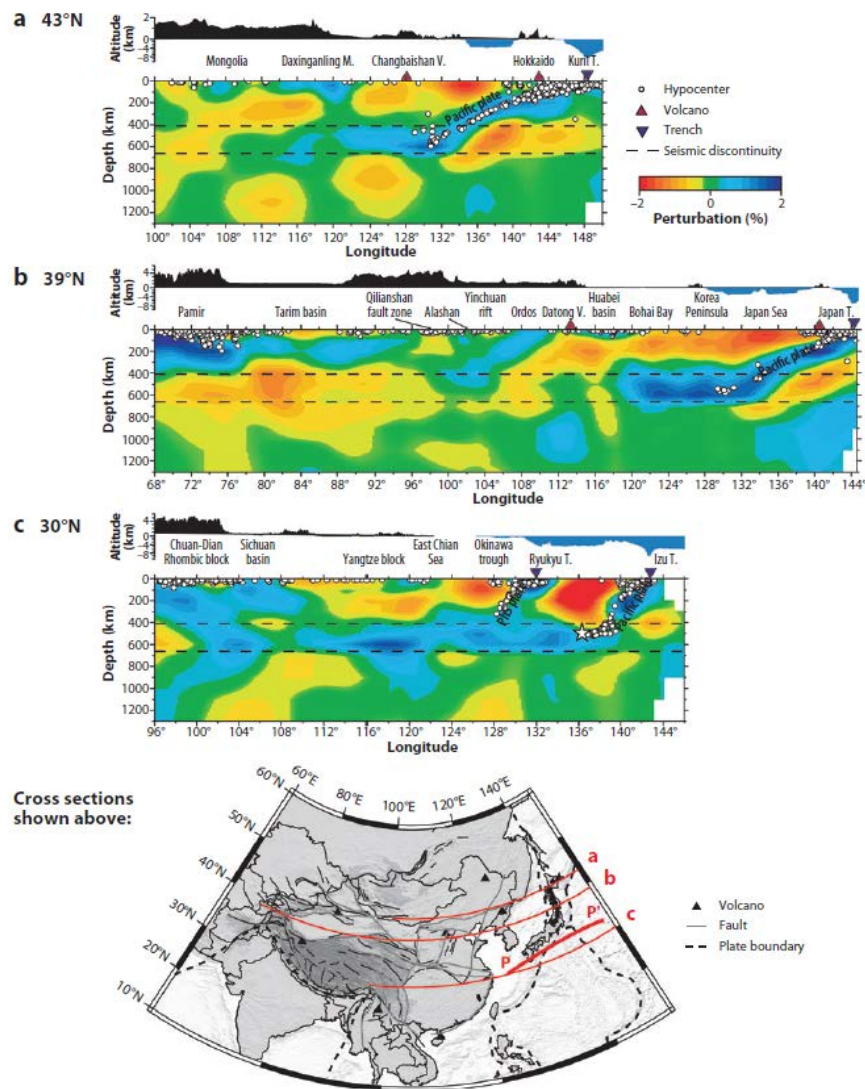


Figure 4.10: East-West vertical cross sections of P-wave velocity perturbations along latitudes 43, 39, and 30, where the horizontal slab (i.e. stagnant slab) extends over a distance of 800 to 1000 km above the 660-km discontinuity. From Fukao et al. (2009).

4.6 References

- Bina, C. & Helffrich, G., 1994. Phase transition Clapeyron slopes and transition zone seismic discontinuity topography, *J. Geophys. Res.*, **99**, 15853-15860.
- Bock, G., 1994. Synthetic seismogram images of upper mantle structure: No evidence for a 520-km discontinuity, *J. Geophys. Res.*, **99**, 15843-15851.
- Christensen, U.R., 1996. The influence of trench migration on slab penetration into the lower mantle, *Earth Planet. Sci. Lett.*, **140**, 27-39.
- Castle, J.C. & Creager, K.C., 1997. Seismic evidence against a mantle chemical discontinuity near 660 km depth beneath Izu-Bonin, *Geophys. Res. Lett.*, **24**, 241-244.
- Cummins, P.R., Kennet, B.L.N., Bowman, J.R. & Bostock, M.G., 1992. The 520-km discontinuity, *Bull. Seismol. Soc. Am.*, **82**, 323-336.
- Deuss, A. & Woodhouse, J., 2001. Seismic observations of splitting of the mid-transition zone discontinuity in Earth's mantle, *Science*, **294**, 354-357.
- Dziewonski, A.M. & Anderson, D.L., 1981. Preliminary Reference Earth Model, *Phys. Earth Planet. Inter.*, **25**, 297-356.
- Escalante, C., Gu, Y.J. & Sacchi, M., 2007. Simultaneous iterative time-domain sparse deconvolution to teleseismic receiver functions, *Geophys. J. Int.*, **171**, 316-325.
- Escalante, C., 2001. Seismic tomography of the SE and Central Brazil, *M.Sc. Dissertation*, University of Sao Paulo, 86 pp. (in Portuguese)
- Fukao, Y., Obayashi, M., Nakakuki, T. & the deep slab project group, 2009. Stagnant slab: a review, *Ann. Rev. Earth Planet. Sci.*, **39**, 291-323.
- Fukao, Y., Widiyantoro, S. & Obayashi, M., 2001. Stagnant slabs in the upper and lower transition region, *Rev. Geophys.*, **39**, 291-323.
- Fukao, Y., Obayashi, M., Inoue, M. & Nenbai, M., 1992. Subducting slabs stagnant in the mantle transition zone, *J. Geophys. Res.*, **97**, 4809-4822.
- Gao, Y., Suetsugu, D., Kujao, Y., Obayashi, M., Shi, Y. & Liu, R., 2010. Seismic discontinuities in the mantle transition zone and at the top of the lower mantle

- beneath eastern China and Korea: Influence of the stagnant Pacific slab, *Phys. Earth Planet Int.*, **183**, 288-295.
- Helfrich, G., 2000. Topography of the transition zone seismic discontinuities, *Rev. Geophys.*, **38**, 141-158.
- Ito, E. & Takahashi, E., 1989. Postspinel transformations in the system Mg_2SiO_4 - Fe_2SiO_4 and some geophysical implications, *J. Geophys. Res.*, **94**, 10637-10646.
- Katsura, T. & Ito, E., The system Mg_2SiO_4 - Fe_2SiO_4 at high pressures and temperatures: precise determination of stabilities of olivine, modified spinel, and spinel, *J. Geophys. Res.*, **94**, 15663-15670.
- Li, C. & van der Hilst, 2010. Structure of the upper mantle and transition zone beneath Southeast Asia from traveltimes tomography, *J. Geophys. Res.*, **115**, B07308, doi:10.1029/2009JB006882.
- Li, X., Sobolev, S.V., Kind, R., Yuan, X. & Estabrook, Ch., 2000. A detailed receiver function image of the upper mantle discontinuities in the Japan subduction zone, *Earth Planet. Sci. Lett.*, **183**, 527-541.
- Nakamura, M., Yoshida, Y., Kuroki, H., Yoshizawa, K., Zhao, D., Takayama, H., Yamazaki, T., Kuroki, H., Yoshizawa, K., Kasahara, J., Kanazawa, T., Kodaira, S., Sato, T., Shiniobara, H. & Hino, R., 2000. Three-dimensional P and S wave velocity structure beneath Japan, *Programme Abstracts*, Seis. Sac. Japan, 2000 Fall meeting, P050. (in Japanese)
- Niu, F., Levander, A., Ham, S. & Obayashi, M., 2005. Mapping the subducting Pacific slab beneath southwest Japan with Hi-net receiver functions, *Earth Planet. Sci. Lett.*, **239**, 9-17.
- Okada, Y., Kasahara, K., Hori, S., Obara, K., Sekiguchi, S., Fujiwara, H. & Yamamoto, A., 2004. Recent progress of seismic observations networks in Japan – Hi-net, F-net, K-NET and KiK-net-, *Earth Planets Space*, **56**, xv-xxviii.
- Ringwood, A., 1994. Role of the transition zone and 660 km discontinuity in mantle dynamics, *Phys. Earth Planet. Int.*, **86**, 5-24.
- Ringwood, A., 1991. Phase-transformations and their bearing on the constitution and dynamics of the mantle, *Geochem. Cosmochem. Acta*, **55**, 2083-2110.

- Ryberg, T., Wenzel, F., Egorkin, A.V. & Solodilov, L., 1997. Short-period observation of the 520 km discontinuity in northern Euroasia, *J. Geophys. Res.*, **102**, 5413-5422.
- Schimmel, M., Assumpcao, M. & VanDecar, J.C., 2003. Seismic velocity anomalies beneath SE Brazil from *P* and *S* wave travel time inversions, *J. Geophys. Res.*, **108**, NO. B4, 2191, doi:10.1029/2001JB000187.
- Schimmel, M., 1999. Phase Cross-Correlations: Design, Comparisons, and Applications, *Bull. Seismol. Soc. Am.*, **89**, 1366-1378.
- Shearer, P.M., 2000. Upper mantle seismic discontinuity, in *Earth's Deep Interior: Mineral Physics and Tomography from the Atomic to the Global Scale*, AGU Geophysical Monograph, Vol. 117, 115–131.
- Shearer, P., Flanagan, M.P. & Hedlin, M.A.H., 1999. Experiments in migration processing of SS precursor data to image upper mantle discontinuity structure, *J. Geophys. Res.*, **104**, 7229-7242.
- Shearer, P.M., 1996. Transition zone velocity gradients and the 520-km discontinuity, *J. Geophys. Res.*, **101**, 3053-3066.
- Shearer, P. M., & Masters, T. G., 1992. Global mapping of topography on the 660 km discontinuity, *Nature*, **355**, 791-796.
- Shearer, P.M., 1991. Constraints on upper mantle discontinuities from observations of long-period reflected and converted phases, *J. Geophys. Res.*, **96**, 18147-18182.
- Shearer, P.M., 1990. Seismic imaging of upper-mantle structure with new evidence for a 520-km discontinuity, *Nature*, **344**, 121-126.
- Shen, Y., Solomon, S.C., Bjarnason, I.T. & Purdy, G.M., 1996. Hot mantle transition zone beneath Iceland and the adjacent Mid-Atlantic Ridge inferred from *P*-to-*S* conversions and the 410- and 660-km discontinuities, *Geophys. Res. Lett.*, **23**, 3527–3530.
- Shen, Y., Sheehan, A.F., Dueker, K.G., de Groot-Hedlin, C. & Gilbert, H., 1998. Mantle discontinuity structure beneath the southern East Pacific Rise from *P*-to-*S* converted phases, *Science*, **280**, 1232–1235.
- Stixrude, L. & Lithgow-Bertelloni, C., 2012. Geophysics of chemical heterogeneity in the mantle, *Annu. Rev. Earth Planet. Sci.*, **40**, 569-595.

- Tonegawa, T., Hirahara, K., Sibutani, T., Iwamori, H., Kanamori, H. & Shiomi, K., 2008. Water flow to the mantle transition zone inferred from a receiver function image of the Pacific slab, *Earth Planet. Sci. Let.*, **274**, 346-354.
- Tonegawa, T., Hirahara, K. & Shibutani, T., 2005. Detailed structure of the upper mantle discontinuities around the Japan subduction zone imaged by receiver function analyses, *Earth Planets Space*, **57**, 5-14.
- Van der Hilst, R.D., Widiantoro, S. & Engdahl, E.R., 1997. Evidence for deep mantle circulation from global tomography, *Nature*, **386**, 578-584.
- Vidale, J.E. & Benz, H.M., 1992. Upper-mantle seismic discontinuities and the thermal structure of subduction zones, *Nature*, **356**, 678-682.
- Wang, X. & Niu, F., 2011. Imaging the mantle transition zone beneath eastern and central China with CEArray receiver functions, *Earthq Sci*, **24**, 65-75.
- Zhong, S. & Gurnis, M., 1997. Dynamic interaction between tectonic plates, subducting slabs, and the mantle, *Earth Interact. 1*, 1-18.

CHAPTER 5

CONCLUSIONS

5.1 Conclusions

In an attempt to bring more information about the mantle transition zone and the fate of the subducting plate beneath Japan, an alternative approach to existing methods to compute high-resolution receiver function has been introduced in this thesis. This new method, so-called sparse deconvolution, improves the deconvolution by using reweighting strategies based on a Cauchy criterion. The resulting sparse receiver functions enhance the primary converted phases and its multiples. To test its functionality and reliability, a series of synthetic experiments and applications to real seismological data were conducted. The results clearly demonstrate that the simultaneous iterative time-domain sparse deconvolution is a suitable method for the determination of high-resolution teleseismic receiver functions (Escalante *et al.*, 2007).

The sparse deconvolution technique for computing teleseismic receiver functions was finally employed to obtain a high resolution image of the topography of the mantle transition zone discontinuities beneath Japan. More than 9,500 waveforms with good signal-to-noise ratios were selected for computing the sparse receiver functions. Furthermore, to preserve coherence of the travel time picking and source time window, a multichannel phase cross-correlation technique (Schimmel 1999, 2003; Escalante, 2012, 2001) was adapted to determine relative arrival

times. Based on the relative times, a more consistent source time window for computing the sparse receiver functions was selected. This is particularly important, as many waveforms, corresponding to different seismic events, are simultaneously used to estimate each sparse receiver function. The results show a locally elevated 410-km discontinuity with a topographic relief of up to 10 km in a region coincident with the subducting Pacific plate. Conversely, the 660-km discontinuity shows a significant large depression of up to ~30 km, well in agreement with the stagnation of the Pacific plate at these depths. These results are consistent with previous receiver function studies and with global tomographic images of a flat lying slab in this region. It is still debatable whether parts of the deflected slab is sinking into the lower mantle or not; since this is not really clear from our observations. But it appears that the 660-km discontinuity deflection extends further to the west into the Korean Peninsula.

5.2 Future Work

Even though the results presented in this thesis nicely complement the ongoing effort in providing a high-resolution image for seismic structure and discontinuity mapping beneath Japan, there are still many open questions and aspects that need to be further investigated. For instance, the sparse receiver functions presented in this thesis, and in general all the methods for computing receiver functions, are conducted under the assumption of isotropic medium, which is not the case for a complex tectonic region such as Japan, where significant anisotropy has been observed in several studies. Future work could include the effects of anisotropy within the receiver functions. This can be accomplished by analyzing transverse

receiver functions which can also be computed by the sparse deconvolution approach.

Additionally, in recent years, advances on signal and image processing have shown better and more efficient regularization schemes, than the Cauchy norm used in this research. For instance, the sparse optimization using L_1 norm has proved to be efficient in producing the sparsest solution under certain conditions (Donoho, 2006). The L_1 norm utilizes the absolute value of the model parameters and tends to promote larger values and fewer smaller values in the model than other regularization approaches when minimized. As a result its solution naturally becomes sparser and thus higher resolution (Bonar, 2010; Donoho, 2006; Beck and Teboulle, 2009). Implementation of the L_1 norm could potentially further benefit the estimation of teleseismic receiver functions.

5.3 References

- Beck, A. & Teboulle, M., 2009. A fast iterative shrinkage thresholding algorithm for linear inverse problems, *SIAM J. Imaging Sciences*, **2**, 183-202.
- Bonar, D., 2012, Sparsity and group sparsity constrained inversion for spectral decomposition of seismic data, *MSc. Dissertation*, University of Alberta, 121 pp.
- Donoho, D., 2006. For most large underdetermined systems of linear equations, the minimal L_1 norm solution is also the sparsest solution, *Communications on Pure and Applied Mathematics*, **59**, 797-829.
- Escalante, C., Gu, Y.J. & Sacchi, M., 2007. Simultaneous iterative time-domain sparse deconvolution to teleseismic receiver functions, *Geophys. J. Int.*, **171**, 316-325.

- Escalante, C., Heimpel, M. & Sacchi, M., 2012. High-resolution imaging of the mantle transition zone discontinuities beneath Japan from sparse receiver functions, in preparation for publication *Earth, Planets and Space*.
- Escalante, C., 2001. Seismic tomography of the SE and Central Brazil, *M.Sc. Dissertation*, University of Sao Paulo, 86 pp. (in Portuguese)
- Schimmel, M., Assumpcao, M. & VanDecar, J.C., 2003. Seismic velocity anomalies beneath SE Brazil from *P* and *S* wave travel time inversions, *J. Geophys. Res.*, **108**, NO. B4, 2191, doi:10.1029/2001JB000187.
- Schimmel, M., 1999. Phase Cross-Correlations: Design, Comparisons, and Applications, *Bull. Seismol. Soc. Am.*, **89**, 1366-1378.

APPENDIX A

F-NET BROADBAND SEISMOGRAPH NETWORK

Station	Latitude	Longitude	Altitude (m)	Depth up to seismometers (m)	Overburden (m)	Sensor
ABU	34.8635	135.5706	137	166	60	STS-1
ADM	37.9046	138.4303	275	35	35	STS-2
AMM	28.1571	129.3001	12	58	43	STS-1
AOG	32.4508	139.774	84	20	43	STS-2
ASI	36.6342	139.4206	663	48	30	STS-2
CHS	35.7055	140.8517	52			STS-2
FUJ	35.2307	138.4181	618		40	STS-1
FUK	32.7177	128.7572	75	29	28	STS-1
GJM	39.9555	140.1113	105	15	10	STS-1
HID	42.8208	142.4145	228	230	90	STS-2
HJO	33.1048	139.8024	87	35	44	STS-2
HKW	35.0965	138.1349	449			STS-2
HRO	37.2246	140.8777	615	46	24	STS-2
HSS	42.9672	141.2286	220		25	STS-1
IGK	24.4131	124.1808	77	47	23	STS-2
IMG	42.3928	140.1406	50	28	15	STS-2
INN	33.4701	131.3062	168	27	24	STS-2
ISI	34.0606	134.4554	27	64	14	STS-1
IWT	35.929	139.7349	6			STS-2
IYG	40.1217	141.5833	427	48	35	STS-2
IZH	34.1359	129.2065	384	48	25	STS-2
JIZ	34.9166	138.9938	263	42	35	STS-2
KFU	35.7426	138.5658	590			STS-2
KGM	26.7567	128.2153	102	46	30	STS-2
KIS	33.5155	135.5327	66	75	70	STS-1
KMT	33.6782	135.4899	152	35	29	STS-2
KMU	42.2391	142.9625	177	23	10	STS-2
KNM	35.7168	137.1781	338	49	32	STS-2
KNP	43.7625	143.7084	158	43	27	STS-2
KNY	34.8738	138.0628	258	46	36	STS-2
KSK	38.2585	140.5833	318	47	40	STS-2
KSN	38.9762	141.5301	260	23	30	STS-2
KSR	42.982	144.4851	17	35	18	STS-2
KYK	30.3781	130.4099	310	16	13	STS-2
KZK	37.2977	138.5143	250	79	60	STS-1
KZS	34.2056	139.1485	191	35	46	STS-2
MMA	41.1619	140.4107	80	28	23	STS-2
NAA	35.2239	137.3622	200	100	65	STS-1

Station	Latitude	Longitude	Altitude (m)	Depth up to seismometers (m)	Overburden (m)	Sensor
NKG	44.8017	142.0849	30	35	24	STS-2
NMR	43.3673	145.7379	20	17	8	STS-2
NOK	34.1656	135.3478	94	48	34	STS-2
NOP	44.3218	142.9384	125	34	25	STS-2
NRW	34.7682	133.5325	199	46	46	STS-2
NSK	34.3403	132.0018	211	150	65	STS-2
OHS	34.6858	138.0122	68			STS-2
OKW	33.8272	133.4691	827	34	50	STS-1
ONS	36.1557	138.9822	478	48	32	STS-2
OOW	40.4689	140.5097	205	35	26	STS-2
OSW	27.0983	142.1961	11	54	42	STS-2
SAG	36.2553	133.3049	70	35	37	STS-2
SBR	33.5052	130.253	260	29	28	STS-1
SBT	37.9683	139.4501	130	33	30	STS-1
SGN	35.5096	138.9443	785	16	20	STS-1
SHR	44.0563	144.9944	110	35	27	STS-2
SIB	31.9698	130.3486	655	15	10	STS-2
SMZ	34.9904	138.5136	0			STS-2
SRN	36.2017	136.6303	472	35	40	STS-2
STM	32.887	129.7237	144	35	44	STS-2
TAS	31.1945	130.9093	504	48	39	STS-2
TGA	35.1847	136.3382	297	48	51	STS-2
TGW	33.9734	132.9319	299	49	50	STS-2
TKA	31.516	130.783	535		5	STS-1
TKD	32.8179	131.3875	749	29	24	STS-2
TKO	31.8931	131.2321	88	9	8	STS-2
TMC	32.6063	130.9151	283	48	60	STS-2
TMR	41.1016	141.3831	120	33	20	STS-1
TNK	44.7779	142.0791	60			STS-1
TNR	34.9111	137.8822	140			STS-2
TSA	33.1781	132.82	141	46	42	STS-2
TSK	36.2141	140.0898	173	56	41	STS-1
TTO	35.8363	138.1209	1149	28	23	STS-1
TYM	34.9745	139.8449	22		48	STS-1
TYS	39.3772	141.5932	346	50	32	STS-2
UMJ	33.5795	134.0367	361	47	57	STS-2
URH	42.9298	143.6711	80	44	34	STS-1
WJM	37.4021	137.0257	200	35	28	STS-2
WTR	34.3739	136.5747	94	48	32	STS-2
YAS	35.657	135.1604	231	47	45	STS-2
YMZ	36.9267	140.2445	520	35	40	STS-1
YNG	24.455	123.007	83	35	20	STS-2
YSI	35.1942	132.8862	385	48	42	STS-2
YTY	34.2835	131.0364	155	49	30	STS-2
YZK	35.0887	134.4594	329	40	34	STS-2
ZMM	26.2328	127.3038	21	20	16	STS-2